國立臺灣大學理學院物理學研究所

碩士論文

Graduate Institute of Physics

College of Science

National Taiwan University

Master Thesis

應用於熱電之立方摻銻碲化鍺化合物之第一原理研究

First-Principles Studies of Cubic Sb-Doped GeTe Compounds for Thermoelectric Applications

張光遠

Benjamin K Chang

指導教授：周美吟博士

Advisor: Mei-Yin Chou, Ph.D.

中華民國 106 年 6 月

June, 2017

doi:10.6342/NTU201701378

國立臺灣大學碩士學位論文
口試委員會審定書

應用於熱電之立方摻銻碲化鍺化合物之第一原理研究

First-Principles Studies of Cubic Sb-Doped GeTe Compounds for Thermoelectric Applications

本論文係張光遠君（R04222010）在國立臺灣大學物理學系、所完成之碩士學位論文，於民國 106 年 6 月 12 日承下列考試委員審查通過及口試及格，特此證明

口試委員：

______________________（簽名）

（指導教授）

__________ __________

__________ __________

__________ __________

__________ __________

致謝

念了碩士才發現這不是件容易的事，更不是件可以自己獨立完成的事。感謝家人在我的成長過程中帶給我的影響，是你們讓我堅定的走上學術之路。尤其感謝我母親，不管是我心裡有什麼樣的苦惱和猶豫，妳說的話總是可以讓它們迎刃而解。感謝我的女朋友楊妤婷，妳自己身在外地工作、加班、為自己的未來打拼之餘，總還可以撥出心力支持我，甚至在我身體不適時放下一切來照顧我。感謝周美吟老師對我的細心指導以及各方面的大力提拔，沒有周老師，我無法完成這份研究，也難以繼續追逐自己的夢想。感謝陳貴賢老師以及 Deniz P. Wong 博士給與我珍貴的合作機會，使我可以同時奠定理論及實驗的基礎。感謝李弘文博士、邢正蓉博士、Duc-Long Nguyen 學長、褚志彪博士、及詹楊皓博士，你們總是在我計算卡關的時候出手相救。感謝謝子祺學長、邢家維學長、呂驊樵學長、潘祈叡學長、徐豪學長、以及侯宗誠學長，你們熱情並有耐心的招待初出茅廬的我，同時總是給研究室帶來歡笑。最後感謝王書偉、吳攸彌、李彥頲、及林合俊，有同年的你們互相照應真的是相當幸運，希望將來我們也有機會繼續一起打拼和學習。感謝這些人，我才會成為今天的我，也才可以順利的取得碩士學位，完成我夢想的一角。感謝你們。

doi:10.6342/NTU201701378

中文摘要

鍺銻碲化合物 (Ge-Sb-Te compound) 因其相變的特質，最早被應用於非揮發性記憶體 [47]。近年來，該類化合物應用於熱電 (thermoelectric) 方面的可能性亦被探討。經實驗上證實，經由適當的製程方式，該化合物的熱電優值 (zT) 可在約攝氏 300 度的操作環境下增加至 2.5 以上，表現極佳 [45]。

本研究旨在使用第一原理計算，以立方碲化鍺 (cubic GeTe) 晶體為基底，探討立方銻碲鍺化合物的晶體結構、電子結構、傳輸性質，以及銻在該化合物中扮演的角色。我們首先說明了立方碲化鍺極易產生鍺空缺 (Ge vacancies) 和銻取代缺陷 (Sb substitutions) 以形成銻碲鍺化合物。接著，我們發現銻碲鍺化合物能在存在大量缺陷之情況下維持晶體結構之穩定性。而後，我們發現該系統的能帶結構在有大量缺陷的情況下，仍可與完美的立方碲化鍺晶體之能帶結構相去不遠。這些證據說明，缺陷在鍺銻碲化合物中扮演調整費米能級的功能。也因為如此，我們提出剛性能帶模型，利用完美的立方碲化鍺晶體之能帶結構進行波茲曼方程式的計算，以估計鍺銻碲化合物的傳輸性質。最後，在與實驗結果比對後，我們推測：對於鍺銻碲薄膜，其生長的基板可能是決定其熱電性質的一大重要因素。

銻碲鍺化合物是極有潛力的熱電材料，本研究為未來該化合物方面的研究奠定了基礎。

關鍵字：熱電、能量學、能帶展開、剛性能帶模型、波茲曼傳輸理論、第一原理

doi:10.6342/NTU201701378

Abstract

Ge-Sb-Te (GST) compounds have been known for their application to non-volatile memories due to their good phase change property [47]. Recently, their applicability to thermoelectric usage has also been discussed. It has been shown that by proper preparation procedures, their thermoelectric figure of merit (zT) can be boosted over 2.5 near 300°C [45].

In this study, we adopt first-principles calculations and use cubic-phase GeTe as an example to investigate the crystal structure, electronic structure, transport properties, and the role of Sb in cubic GST. First, we show that a considerable amount of Ge vacancies and Sb substitutions are both easily introduced into cubic GeTe to form cubic GST. Second, we find that the crystal structure of cubic GST can sustain a large amount of defects. Third, we show that the band structure of cubic GST remains similar to that of cubic GeTe in the presence of many defects. These findings indicate that the role of the defects in GST is largely tuning the Fermi level. Thus, we adopt a rigid band model and use the cubic GeTe band structure to estimate the transport properties of cubic GST. Finally, by directly comparing our calculational results to experiment results, we conclude that the substrate plays a substantial role in determining the transport properties of GST thin films.

GST is a very promising type of thermoelectric materials. We believe that this study provides a guideline for the future development on GST.

Key words: thermoelectric, energetics, band unfolding, rigid band model, Boltzmann transport theory, first-principles

doi:10.6342/NTU201701378

Contents

口試委員會審定書 i

致謝 ii

中文摘要 iii

Abstract iv

Contents v

List of Figures viii

List of Tables x

1 Introduction 1

1.1 Thermoelectric materials 1

1.2 Antimony-doped germanium tellurides 2

2 Computational Methodology 5

2.1 First-principles calculations 5

2.2 Band unfolding 6

2.2.1 Band visualization problem 6

2.2.2 Band unfolding principles 6

2.3 Transport property calculations 7

2.3.1 Introduction 7

2.3.2 Quantities of interest 8

doi:10.6342/NTU201701378

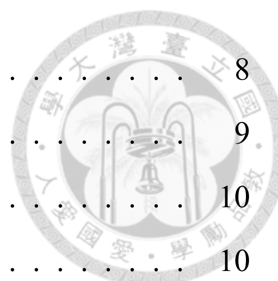

2.3.3 Boltzmann equation 8

2.3.4 Relaxation time approximation 9

2.3.5 Temperature gradient 10

2.3.6 Expressions of transport quantities 10

3 Theoretical analysis of cubic GST system 12

3.1 Introduction 12

3.2 Electronic structure of β-GeTe 15

3.3 Energetics 15

3.3.1 Configuration of a V_{Ge} and a S_{Sb} 15

3.3.2 Formation of defects 15

3.3.3 Formation of a S_{Sb} in V_{Ge}-rich environment 16

3.3.4 Summary of the energetics 18

3.4 Structural relaxation 18

3.4.1 Single defect induced relaxation 18

3.4.2 Relaxation induced by the combination of V_{Ge} and S_{Sb} 20

3.4.3 Summary of relaxation analysis 20

3.5 Unfolded band structures 21

3.5.1 Electron counting 21

3.5.2 Band structure with defects 22

3.5.3 Band structure with both V_{Ge} and S_{Sb} 25

3.5.4 Quantitative measure of band rigidity 26

3.5.5 Summary of unfolded bands 26

3.6 Boltzmann theory calculations and direct comparison to experiment data . 28

3.6.1 Experimental results by Wong *et al*. [45] 28

3.6.2 Seebeck coefficient 29

3.6.3 Carrier concentration 29

3.6.4 Relaxation time 30

3.6.5 Summary of transport calculations and speculation on the substrate 32

3.7 Conclusion 33

doi:10.6342/NTU201701378

A **34**

A.1 High symmetry points 34

A.2 Valence electrons used in DFT calculation 35

A.3 Supercells used in Sec. 3.5.2 35

A.4 Fermi level scanning 36

Bibliography **37**

doi:10.6342/NTU201701378

List of Figures

3.1 The conventional cell of cubic rocksalt structure β-GeTe ($Fm\bar{3}m$ group), where the purple balls are Ge atoms, and the yellow balls are Te atoms. . 12

3.2 The band structure of β-GeTe with projections onto **(a)** Ge s- and p-orbitals, and **(b)** Te s- and p-orbitals. The high symmetry points according to which the band structure is drawn are defined in A.1. 13

3.3 The density of states (DOS) for β-GeTe, where **(a)** shows the projections onto Ge s- and p-orbitals, **(b)** is the projections on Te s- and p-orbitals. The black curves are the total DOS. 14

3.4 Illustration of the atomic arrangements for the calculations of V_{Ge}-rich environment. i is the index used in Table. 3.2. 17

3.5 Structural relaxation of a $4 \times 4 \times 4$ SC in the presence of **(a)** a single V_{Ge} (black ball) at the center, and **(b)** a single S_{Sb} (orange ball) at the center. . 19

3.6 Structural relaxation of a $4 \times 4 \times 4$ SC in the presence of a V_{Ge} and a S_{Sb}. 20

3.7 Unfolded bands for **(a)** 3×3×3 SC **(b)** 2×3×3 SC **(c)** 2×2×3 SC **(d)** 2×2×2 SC, each containing one V_{Ge}. 23

3.8 Unfolded bands for **(a)** 3×3×3 SC **(b)** 2×3×3 SC **(c)** 2×2×3 SC **(d)** 2×2×2 SC, each containing one S_{Sb}. 24

3.9 **(a)** Unfolded bands of the $2V_{Ge}^{1}$ SC from Table 3.2. **(b)** Zoom-in band structure of β-GeTe for comparison. 25

3.10 Fermi level versus number of electrons per chemical formula of each SC. 27

3.11 Seebeck coefficient as a function of temperature. "Exp." is the measured Seebeck coefficient of the GST thin flims provided by Wong *et al*. [45] . 29

doi:10.6342/NTU201701378

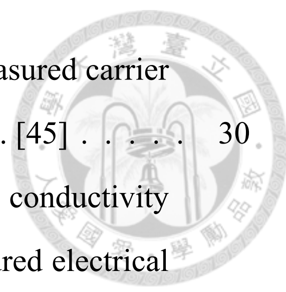

3.12 Carrier concentration versus temperature. "Exp." is the measured carrier concentration of the GST thin flims provided by Wong *et al*. [45] 30
3.13 The curves labelled with "eV" are the calculated electrical conductivity over relaxation time (σ/τ). "$\sigma_{\text{Exp.}}$" is the data of the measured electrical conductivity of the GST films provided by Wong *et al*. [45] 31
3.14 The curves labelled with "eV" are the computed electronic thermal conductivity over relaxation time (κ_{ele}/τ). "$\kappa_{\text{tot,Exp.}}$" is the data of the measured total conductivity of the GST films provided by Wong *et al*. [45]. . 32

doi:10.6342/NTU201701378

List of Tables

3.1 Total energies of SC and creation energies of defects (eV). 16

3.2 Creation energy of S_{Sb} in the presence of two V_{Ge} (eV). 17

3.3 Displacement data for the atoms on Cartesian axes in Fig. 3.5. 19

3.4 Root-mean-square deviation per energy eigenvalue for the unfolded spectra. The unit is in eV. 27

doi:10.6342/NTU201701378

Chapter 1

Introduction

1.1 Thermoelectric materials

Energy usage is crucial for the human society. While electricity is a form of energy that can be well manipulated and exploited by current technologies, heat is still often uncontrollable and hard to make use of. Thermoelectric materials provide a way to alleviate this problem [4,51]. Through the Seebeck effect [43], thermoelectric materials are capable of generating electrical current (or voltage) with the presence of a temperature gradient. In other words, they can transform heat into electricity.

For a thermoelectric material to have a favourable energy conversion efficiency, one usually wants it to fulfil three requirements. First, large Seebeck coefficient (S)—in order to achieve larger voltage per unit temperature gradient; second, large electrical conductivity (σ)—in order to have more current generated per voltage; and third, small thermal conductivity (κ)—in order to maintain the temperature imbalance of the system. All of these requirements can be summarized as a measure of the dimensionless thermoelectric figure of merit, which is defined as

$$zT = \frac{S^2\sigma}{\kappa}T, \tag{1.1}$$

where T is the temperature, and the numerator $P = S^2\sigma$ is called the power factor. Therefore, one wants to create thermoelectric materials with zT as large as possible. However,

doi:10.6342/NTU201701378

note that temperature is one of the factors in zT; this implies that various thermoelectric materials may be suitable for different operating temperature ranges.

While the zT values of conventional thermoelectric materials are often below 1.0 [24, 30, 51], they can be boosted by band structure engineering and thermal conductivity reduction, which are often achieved by proper alloying or doping [1, 43, 51]. The lead telluride (PbTe) based thermoelectric materials are a good example to demonstrate this process of improvement.

PbTe is a IV-VI compound that crystalizes into a cubic rocksalt structure ($Fm\bar{3}m$ group) [3, 10]. First, it was reported that PbTe has a peak zT only near 1.0 at about 650K [10, 13, 30]. However, many kinds of dopants have been explored, such as Tl [15], Mg [12], Na [32], and Se [12, 33]. It was demonstrated that the zT of PbTe can be effectively improved by the doping of additional elements. Moreover, it was reported that bulk PbTe can reach an exceptionally high zT of 2.2 at 800K if doped with Ag and Sb [16]. This result further triggered people's interest in the role of Sb in the PbTe system [9, 17]. Because of the encouraging improvements and the simple crystal structure that facilitates further analysis, PbTe has been a popular base material for thermoelectric research in the past decade.

1.2 Antimony-doped germanium tellurides

Germanium telluride (GeTe), a group IV telluride like PbTe, however, has not received that much of attention. Similar to PbTe, GeTe has a cubic rocksalt structure (β-phase) at high temperature. Nevertheless, GeTe transforms into a rhombohedral phase (α-phase) below 700K [3, 38]. It is noteworthy that Ge vacancies are easily formed in this system, which leads to the highly deviated stoichiometry and p-type behavior in GeTe [11, 22].

The thermoelectric property of GeTe-based materials has recently captured people's interest. It is reported that GeTe can have zT over 0.8 near 720K, and its power factor outperforms other tellurides [22]. To improve its thermoelectric performance, some dopants have been studied for GeTe as well, such as Bi [23, 46], Se [49], and Mn and Sn [50]. The zT value was boosted over 1.1 and even to 1.9 between 720K and 800K [23, 46, 49, 50].

doi:10.6342/NTU201701378

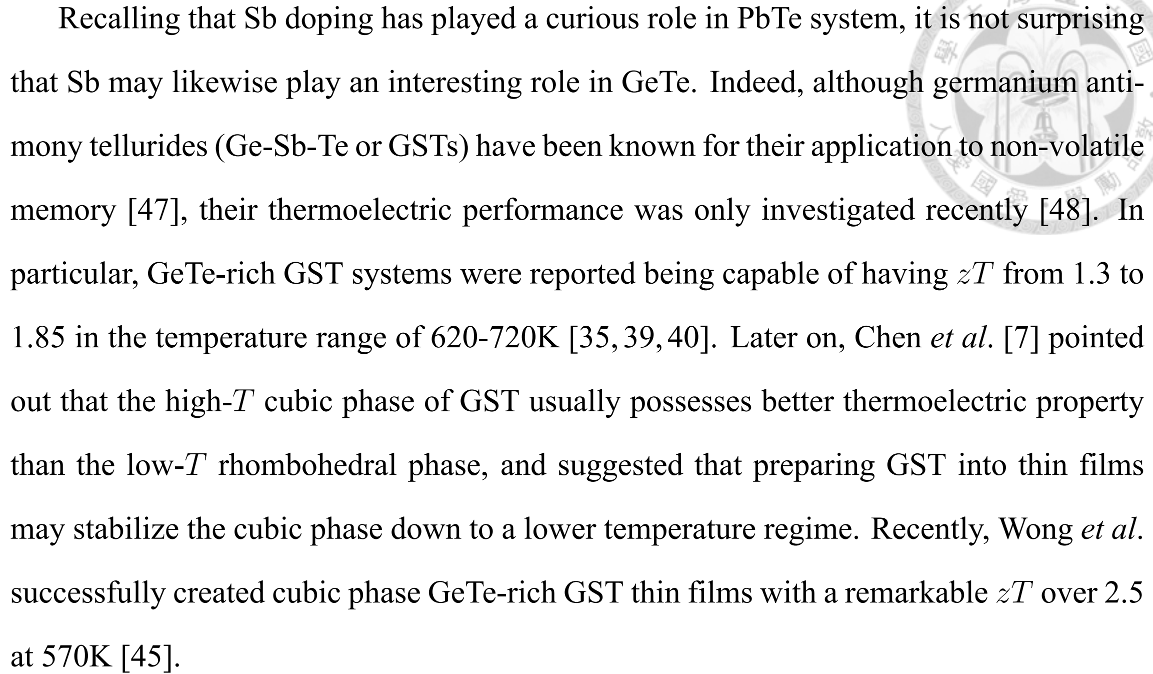

Recalling that Sb doping has played a curious role in PbTe system, it is not surprising that Sb may likewise play an interesting role in GeTe. Indeed, although germanium antimony tellurides (Ge-Sb-Te or GSTs) have been known for their application to non-volatile memory [47], their thermoelectric performance was only investigated recently [48]. In particular, GeTe-rich GST systems were reported being capable of having zT from 1.3 to 1.85 in the temperature range of 620-720K [35, 39, 40]. Later on, Chen *et al*. [7] pointed out that the high-T cubic phase of GST usually possesses better thermoelectric property than the low-T rhombohedral phase, and suggested that preparing GST into thin films may stabilize the cubic phase down to a lower temperature regime. Recently, Wong *et al*. successfully created cubic phase GeTe-rich GST thin films with a remarkable zT over 2.5 at 570K [45].

From the results described above, we see that GST have various advantages in thermoelectric applications. First, the thermoelectric property of GSTs can sometimes surpass that of PbTe. Second, GSTs can function well at lower operating temperature. And third, unlike PbTe, GSTs do not contain toxic elements, reducing the environmental concerns. These merits indicate that GSTs are versatile thermoelectric materials and worth further investigation.

Although GeTe has been well understood, the effect of Sb doping in cubic GST has not been investigated theoretically. Therefore in this work, we use β-GeTe as an example and perform first-principles calculations to investigate the band structure and crystal structure of cubic GST. Since experiment results show that Ge atoms, Ge vacancies (denoted V_{Ge}, V for "vacancy"), and Sb atoms (denoted S_{Sb}, S for "substitution") share the same sites without explicit ordering [7, 8, 26–28, 39, 42], we only consider the cases where both V_{Ge} and S_{Sb} are on Ge-sublattice. Under this setting, we show that V_{Ge} and S_{Sb} favor the presence of each other, which explains the extended stoichiometry observed in experiments [45]. Moreover, we discover that the function of these defects is mainly tuning the Fermi level while leaving the system with GeTe characteristics. Based on these observations, it is demonstrated that the electronic transport properties of cubic GST can be effectively estimated from the β-GeTe electronic structure. Finally, by comparing our

doi:10.6342/NTU201701378

computed results to experiment, we point out the relevance of the substrate to the transport properties of GST films.

doi:10.6342/NTU201701378

Chapter 2

Computational Methodology

2.1 First-principles calculations

Density functional theory (DFT) calculations are performed to investigate atomic relaxations and electronic structures. We use the Vienna *Ab initio* Simulation Package (VASP) [19, 20] with the electron-ion interaction described by projector augmented wave (PAW) [6, 21] pseudopotentials, and the exchange-correlation functional is chosen with the generalized gradient approximation (GGA) [34].

The equilibrium lattice constant of the primitive cell (PC) for cubic GeTe is first obtained, and then supercells (SC) are constructed for further investigation. Spin-orbit coupling (SOC) is not included for atomic relaxation calculations, whereas it is included in all self-consistent calculations. Specifically for the atomic relaxation calculations of SC, cell volumes are constrained. After careful convergence tests, the plane-wave energy cutoff is set to be 200 eV for all calculations, and a Γ-centered $12\times12\times12$ Monkhorst-Pack grid is adopted for the k-mesh of PC calculations. The k-meshes for SC calculations are then obtained by scaling directly from the PC k-mesh. For example, a $2\times3\times3$ SC will be calculated with a Γ-centered $6\times4\times4$ Monkhorst-Pack grid.

doi:10.6342/NTU201701378

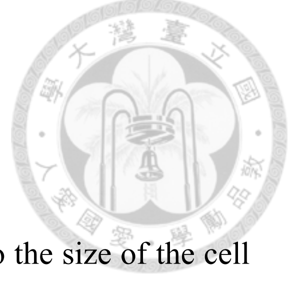

2.2 Band unfolding

2.2.1 Band visualization problem

The size of first Brillouin zone (FBZ) is inversely proportional to the size of the cell to which it corresponds. In particular, SC FBZ are smaller than that of $(1\times1\times1)$ PC, so that the SC bands will look like they are "folded", causing difficulty in visualizing and comparing band structures.

To tackle this problem, we use the state-of-the-art zone-unfolding technique as implemented in the BandUP [29] code to obtain the representation of SC bands in PC FBZ. The method was originally proposed by Popescu and Zunger in Ref. [37]. We will briefly introduce the main idea in the next subsection.

2.2.2 Band unfolding principles

According to Bloch's theorem [2], for a periodic quantum system described by a given unit cell, its eigenstates can be sufficiently characterized by two quantum numbers: n, the "band index", and $\mathbf{k}$, the "crystal momentum vector" that lies in the FBZ defined from that unit cell.

Suppose that a commensurate SC is constructed using a PC lattice. That is, the PC lattice vectors $\{\mathbf{a}_i\}$ and the SC lattice vectors $\{\mathbf{A}_j\}$ are related through an invertible transformation matrix $\boldsymbol{M}$ like

$$\begin{pmatrix}\mathbf{A}_1\\ \mathbf{A}_2\\ \mathbf{A}_3\end{pmatrix} = \begin{pmatrix}M_{11} & M_{12} & M_{13}\\ M_{21} & M_{22} & M_{23}\\ M_{31} & M_{32} & M_{33}\end{pmatrix} \cdot \begin{pmatrix}\mathbf{a}_1\\ \mathbf{a}_2\\ \mathbf{a}_3\end{pmatrix}, \quad M_{ij} \in \mathbb{Z}. \tag{2.1}$$

Let $\{|\mathbf{k}_i n\rangle\}_{i,n}$ and $\{|\mathbf{K}_j m\rangle\}_{jm}$ be the sets of eigenstates for the PC system and the SC system, respectively. It can then be shown that for any j, $|\mathbf{K}_j m\rangle$ can be expressed as a linear combination of $|\mathbf{k}_i n\rangle$ [5, 44]. That is,

$$|\mathbf{K}_j m\rangle = \sum_{i,n} F(\mathbf{k}_i, n; \mathbf{K}_j, m)|\mathbf{k}_i n\rangle \quad \forall j, \tag{2.2}$$

doi:10.6342/NTU201701378

where $F(\mathbf{k}_i, n; \mathbf{K}_j, m)$ is the contribution to $|\mathbf{K}_j m\rangle$ from $|\mathbf{k}_i n\rangle$.

We now seek a way to map the calculated $|\mathbf{K}_j m\rangle$ onto the PC FBZ. Since from Eq. 2.2, it is obvious that a $|\mathbf{K}_j m\rangle$ corresponds to multiple $|\mathbf{k}_i n\rangle$, the mapping is expected to be a weighted one-to-many mapping. We can first define a spectral weight function as

$$P_{\mathbf{K}_j m}(\mathbf{k}_i) = \sum_n |\langle \mathbf{K}_j m | \mathbf{k}_i n \rangle|^2, \tag{2.3}$$

which represents the contribution of $|\mathbf{K}_j m\rangle$ to a specific $\mathbf{k}_i$. We then define the spectral function,

$$A_{\mathbf{K}_j}(\mathbf{k}_i, E) = \sum_m P_{\mathbf{K}_j m}(\mathbf{k}_i)\delta(E_m(\mathbf{K}_j) - E), \tag{2.4}$$

where $E_m(\mathbf{K}_j)$ denotes the energy eigenvalue of $|\mathbf{K}_j m\rangle$. This spectral function reflects the amount of contribution from the SC eigenstates at $\mathbf{K}_j$ in the SC FBZ to *any* point $(\mathbf{k}_i, E)$ in the PC FBZ. By summing over spectral functions of every $\mathbf{K}_j$,

$$A(\mathbf{k}_i, E) = \sum_j A_{\mathbf{K}_j}(\mathbf{k}_i, E), \tag{2.5}$$

we then recover the effective SC band structure in PC FBZ, where the "intensity" $A(\mathbf{k}_i, E)$ indicates the contribution from *all* SC eigenstates to the point $(\mathbf{k}_i, E)$.

2.3 Transport property calculations

2.3.1 Introduction

When it comes to thermoelectric materials, transport properties are especially of our interest. Here we adopt Boltzmann theory calculations as implemented in the BoltzTraP [25] code to determine the *electron-contributed* transport properties with a given band structure, Fermi level, and temperature. Note that since these calculations involve considerable amount of approximations, it is usually considered satisfactory if the computed values and experimentally measured values agree within the same order of magnitude. We will briefly

doi:10.6342/NTU201701378

introduce how to compute the transport quantities in the following. For more details, one can see Ref. [2, 14, 52].

2.3.2 Quantities of interest

In the presence of a temperature gradient ∇T and an electric field **E**, the electric current density **J** and the electronic heat current density **Q** of a system can be written as [2, 14, 25, 36, 41]:

$$\mathbf{J} = \boldsymbol{\sigma}(\mathbf{E} - \boldsymbol{S}\nabla T), \tag{2.6a}$$

$$\mathbf{Q} = T\boldsymbol{\sigma}\boldsymbol{S}\mathbf{E} - \boldsymbol{K}\nabla T, \tag{2.6b}$$

where $\boldsymbol{\sigma}$, $\boldsymbol{S}$ and $\boldsymbol{K}$ (not to be confused with the $\mathbf{K}_j$ in section 2.2.2) are rank-two tensors. Here, $\boldsymbol{\sigma}$ is the electrical conductivity, $\boldsymbol{S}$ is the Seebeck coefficient, and the electronic thermal conductivity is defined as the heat current density per unit temperature gradient in the absence of a charge current:

$$\boldsymbol{\kappa}_e = -\left.\frac{\partial \mathbf{Q}}{\partial(\nabla T)}\right|_{\mathbf{J}=0} = \boldsymbol{K} - T\boldsymbol{\sigma}\boldsymbol{S}^2. \tag{2.7}$$

These transport quantities can be measured directly in experiment, hence we aim for estimating them from calculations.

2.3.3 Boltzmann equation

When a system is in thermal equilibrium at temperature T, the electron occupation follows the Fermi-Dirac distribution:

$$f_0(E_n(\mathbf{k}), \mu, T) = \frac{1}{e^{(E_n(\mathbf{k})-\mu)/k_B T} + 1}, \tag{2.8}$$

where n is the band index and $\mathbf{k}$ is the electron wave vector. However, transport properties occur when a system is out of thermodynamic equilibrium, hence the electron occupation is perturbed from Fermi-Dirac distribution.

doi:10.6342/NTU201701378

A naïve semiclassical approach to this situation is to assume that the system will be driven into a *stationary* (instead of equilibrium) distribution by electron collisions [2]. The Boltzmann theory then states that, for a state $|\mathbf{k}n\rangle$, the stationary nonequilibrium distribution at position **r** and time t should satisfy the Boltzmann equation:

$$\frac{\partial f}{\partial \mathbf{r}} \cdot \mathbf{v}(n, \mathbf{k}) + \frac{1}{\hbar}\frac{\partial f}{\partial \mathbf{k}} \cdot \mathbf{F} + \frac{\partial f}{\partial t} = \left[\frac{\partial f}{\partial t}\right]_{coll}, \tag{2.9}$$

where $[\partial f/\partial t]_{coll}$ is the collision term,

$$\mathbf{v}(n, \mathbf{k}) = \frac{1}{\hbar}\frac{\partial E_n(\mathbf{k})}{\partial \mathbf{k}} \tag{2.10}$$

is the group velocity of electrons, and **F** is the external force. If the external force is provided by an electric field **E**, then

$$\mathbf{F} = -e\mathbf{E} \tag{2.11}$$

Some points regarding Eq. 2.9 should be noted. First, f should have the quantum numbers $(n, \mathbf{k})$ as its arguments. Second, the equation can be evaluated for every **r**, n, **k** and t. Third, the equation does not take into account interband transitions.

We will next explain how to cast Eq. 2.9 into a more favourable form.

2.3.4 Relaxation time approximation

There is a problem with Eq. 2.9, which is the unknown of the expression for the collision term $[\partial f/\partial t]_{coll}$. Here we introduce the "relaxation time" approximation, which has been proved to be efficient to counter this problem in many occasions.

In this approximation, if the temperature is assumed uniform throughout the system (note that uniform temperature does not imply thermal equilibrium), then the collision term is approximated as [14]

$$\left[\frac{\partial f}{\partial t}\right]_{coll} = -\frac{f - f_0(E_n(\mathbf{k}), \mu, T)}{\tau_{n\mathbf{k}}(\mathbf{r})}, \tag{2.12}$$

doi:10.6342/NTU201701378

where f_0 is the Fermi-Dirac distribution as defined in Eq. 2.8, and $\tau_{n\mathbf{k}}(\mathbf{r})$ is the semi-empirical relaxation time function which characterizes the time needed for the system to reach f_0 distribution if the external force F is suddenly removed.

With this approximation, the Boltzmann equation Eq. 2.9 is then shaped into a solvable differential equation.

2.3.5 Temperature gradient

In Eq. 2.12, the T in f_0 is independent of position. That is, we are considering a system that is being driven into a stationary nonequilibrium state where temperature is uniform. If we want to consider a system kept in a temperature gradient, slight modification is required.

We now let the temperature become a function of position. Because the Fermi level μ depends on local electron density and local temperature, which both depend on position, μ is also a function of position. The thermal equilibrium Fermi-Dirac distribution function hence becomes *local* [14]:

$$f_0(E_n(\mathbf{k}), \mu(\mathbf{r}), T(\mathbf{r})) = \frac{1}{e^{(E_n(\mathbf{k})-\mu(\mathbf{r}))/k_B T(\mathbf{r})} + 1}. \tag{2.13}$$

By combining Eq. 2.9, Eq. 2.11, Eq. 2.12, and Eq. 2.13, we have the modified Boltzmann equation:

$$\frac{\partial f}{\partial \mathbf{r}} \cdot \mathbf{v}(n, \mathbf{k}) - \frac{e}{\hbar}\frac{\partial f}{\partial \mathbf{k}} \cdot \mathbf{E} + \frac{\partial f}{\partial t} = -\frac{f - f_0(E_n(\mathbf{k}), \mu(\mathbf{r}), T(\mathbf{r}))}{\tau_{n\mathbf{k}}(\mathbf{r})}. \tag{2.14}$$

It is now possible to obtain the distribution function f for a system in the presence of an electric field and a temperature gradient by solving Eq. 2.14.

2.3.6 Expressions of transport quantities

It can be shown that by assuming a small temperature gradient and a small electric field, and using Eq. 2.14 within appropriate approximations, we will derive the following

doi:10.6342/NTU201701378

expressions for the transport tensors [14, 25, 36, 41]:

$$\sigma_{\alpha\beta}(\mu,T) = e^2 \int \mathrm{d}E \left(-\frac{\partial f_0(E,\mu,T)}{\partial E}\right) \Sigma_{\alpha\beta}(E), \tag{2.15a}$$

$$[\boldsymbol{\sigma S}]_{\alpha\beta}(\mu,T) = \frac{e}{T} \int \mathrm{d}E \left(-\frac{\partial f_0(E,\mu,T)}{\partial E}\right) (E-\mu)\Sigma_{\alpha\beta}(E), \tag{2.15b}$$

$$K_{\alpha\beta}(\mu,T) = \frac{1}{T} \int \mathrm{d}E \left(-\frac{\partial f_0(E,\mu,T)}{\partial E}\right) (E-\mu)^2\Sigma_{\alpha\beta}(E), \tag{2.15c}$$

where the α and β are Cartesian indices, and

$$\Sigma_{\alpha\beta}(E) = \frac{1}{\Omega}\sum_{n,\mathbf{k}} \mathrm{v}_\alpha(n,\mathbf{k})\mathrm{v}_\beta(n,\mathbf{k})\tau_{n\mathbf{k}}\delta(E-E_n(\mathbf{k})) \tag{2.16}$$

is the transport distribution function (TDF).

It is inevitable that the calculated transport tensors will contain relaxation time $\tau_{n\mathbf{k}}$, and the determination of $\tau_{n\mathbf{k}}$ is hard and beyond the scope of this thesis. However, we can apply further simplification by assuming a constant relaxation time [25, 36], that is,

$$\tau_{n\mathbf{k}}(\mathbf{r}) = \tau \quad \forall n, \mathbf{r}, \mathbf{k}. \tag{2.17}$$

In this way, although the electrical conductivity $\boldsymbol{\sigma}$ and the electronic thermal conductivity $\boldsymbol{\kappa}_e$ still contain the relaxation time τ, the τ in $\boldsymbol{\sigma}$ and $\boldsymbol{\Sigma}$ in Eq. 2.15b cancel out, so that the Seebeck coefficient $\boldsymbol{S}$ can be derived without ambiguity.

With these equations, we can thus use the band structure of a system to compute its transport properties at a given Fermi level and temperature.

doi:10.6342/NTU201701378

Chapter 3

Theoretical analysis of cubic GST system

3.1 Introduction

To simulate the cubic GST system, we first reproduce the data and PC of β-GeTe, and then construct SC to investigate the influence of the presence of V_{Ge} and S_{Sb} on the crystal structure and electronic structure. In Ref. [11], Edwards *et al.* already had a very detailed discussion of the intrinsic defects in the GeTe system, including vacancies and antisite defects. Some results regarding V_{Ge} in this work will be compared to their work. As for the transport properties, we will make estimates and then extensively compare them to the experimental work on GST thin films by Wong *et al.* in Ref. [45].

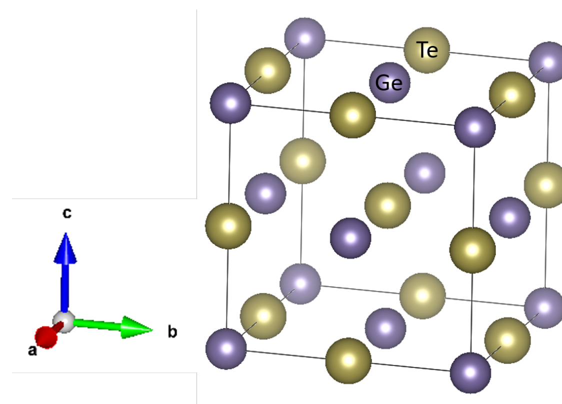

Figure 3.1: The conventional cell of cubic rocksalt structure β-GeTe ($Fm\bar{3}m$ group), where the purple balls are Ge atoms, and the yellow balls are Te atoms.

doi:10.6342/NTU201701378

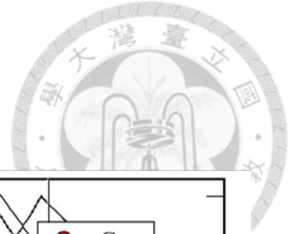

Figure 3.2: The band structure of β-GeTe with projections onto **(a)** Ge s- and p-orbitals, and **(b)** Te s- and p-orbitals. The high symmetry points according to which the band structure is drawn are defined in A.1.

doi:10.6342/NTU201701378

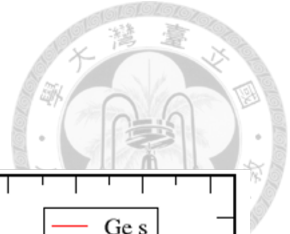

Figure 3.3: The density of states (DOS) for β-GeTe, where **(a)** shows the projections onto Ge s- and p-orbitals, **(b)** is the projections on Te s- and p-orbitals. The black curves are the total DOS.

doi:10.6342/NTU201701378

3.2 Electronic structure of β-GeTe

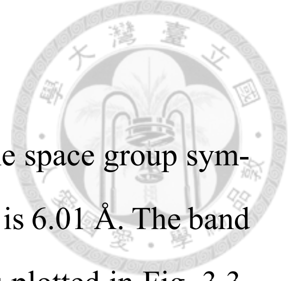

The crystal structure of β-GeTe is illustrated in Fig. 3.1, where the space group symmetry is $Fm\bar{3}m$. The relaxed lattice parameter (for conventional cell) is 6.01 Å. The band structure is plotted in Fig. 3.2, and the (projected) density of states is plotted in Fig. 3.3. All of these are consistent with previous work [11,31,38]. Note that in the following analyses, we will be particularly interested in the bands right below the valence band maxima (VBM). These bands are associated with the p-orbitals of Te atoms as shown in both the projected band structure plot (Fig. 3.2) and the projected density of states plot (Fig. 3.3).

3.3 Energetics

Using the PC obtained in Sec. 3.2, we construct SCs to evaluate the change in the total energy when defects are inserted. The total energies are calculated after the structures are fully relaxed.

3.3.1 Configuration of a V_{Ge} and a S_{Sb}

We first consider the energy dependence on the distance between V_{Ge} and S_{Sb}. We calculate the total energy of a $6 \times 6 \times 6$ SC containing one V_{Ge} and one S_{Sb}, where they are arranged as first to fifth nearest neighbors on the Ge-sublattice. The results suggest that V_{Ge} and S_{Sb} may not have a preferred configuration. This information helps us organize the calculation carried out in the next subsection.

3.3.2 Formation of defects

Here we investigate the formation energies of the defects. A $4 \times 4 \times 4$ SC is adopted, and the total energies of a perfect SC, SC with a single V_{Ge}, SC with a single S_{Sb}, and SC with a V_{Ge}–S_{Sb} pair are calculated and listed in Table. 3.1. The total energy of the perfect SC is obtained by scaling directly from the total energy of PC. In the case where V_{Ge}–S_{Sb} pair is presented, they are arranged as nearest neighbors on the Ge-sublattice for

doi:10.6342/NTU201701378

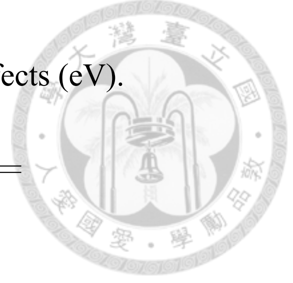

Table 3.1: Total energies of SC and creation energies of defects (eV).

	w/o S_{Sb}	w/ S_{Sb}	ΔE_{sub}
w/o V_{Ge}	-509.175	-508.381	0.79
w/ V_{Ge}	-504.637	-505.269	-0.63
ΔE_{vac}	4.54	3.11	—

convenience. ΔE_{vac} is the formation energy of V_{Ge}, or, the energy needed to remove a Ge atom and place it at infinity. ΔE_{sub} is the formation energy of S_{Sb}, or the substitution energy needed to change a Ge atom into a Sb atom.

Our result shows that it is more likely to form V_{Ge} in the presence of S_{Sb}, since ΔE_{vac} will be reduced by 1.43 eV. Or, we can interpret the data in the way that a Ge atom is inclined to be substituted with a Sb atom when a V_{Ge} is nearby, for the substitution energy ΔE_{sub} turns from positive to negative. These evidences indicate that V_{Ge} and S_{Sb} enhance the presence of each other in GeTe system.

3.3.3 Formation of a $\mathbf{S_{Sb}}$ in $\mathbf{V_{Ge}}$-rich environment

We are interested in the substitution energy ΔE_{sub} in the presence of two V_{Ge}. A $4\times4\times4$ SC containing two V_{Ge} is calculated. Note that there are many possible configurations for the two V_{Ge}. Here we select a site on Ge-site as the central site, and consider only the cases where both V_{Ge} are arranged as nearest neighbors (on the Ge-sublattice) of the central site. Each case is labeled by $2V_{Ge}^{i}$, where a larger i indicates a larger distance between the two V_{Ge}. We then compute the total energy for each case with the central site being either Ge or a substituted Sb. The method of configuration is illustrated in Fig. 3.4, and the energies are listed in Table. 3.2.

In general, the result shows that the presence of S_{Sb} can decrease the total energy of V_{Ge}-rich GeTe system. In other words, although V_{Ge} is already a somewhat easily formed intrinsic defect in GeTe, S_{Sb} can further stabilize them and make the system tolerate even more V_{Ge}. Note however that the case $2V_{Ge}^{4}$ shows that the presence of S_{Sb} will increase

doi:10.6342/NTU201701378

Table 3.2: Creation energy of S_{Sb} in the presence of two V_{Ge} (eV).

$2V_{Ge}^{i}$	w/o S_{Sb}	w/ S_{Sb}	ΔE_{sub}
$2V_{Ge}^{1}$	-499.864	-500.410	-0.55
$2V_{Ge}^{2}$	-499.616	-500.019	-0.40
$2V_{Ge}^{3}$	-499.940	-500.376	-0.44
$2V_{Ge}^{4}$	-499.873	-499.632	0.24

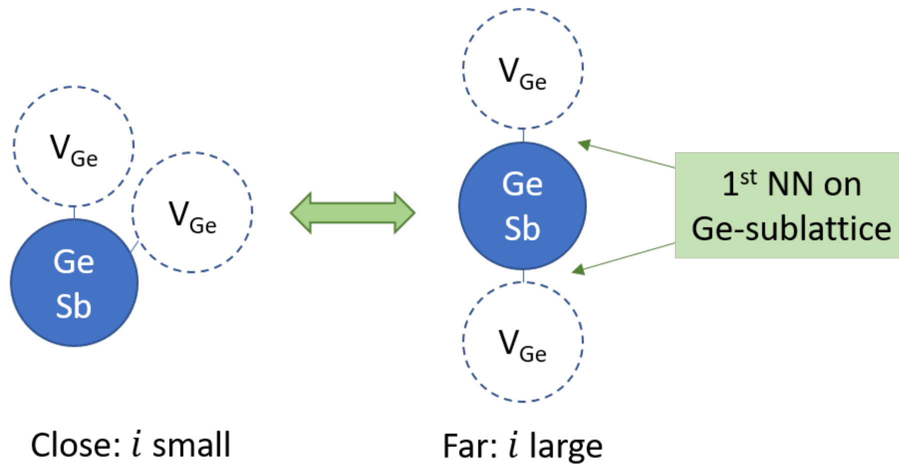

Figure 3.4: Illustration of the atomic arrangements for the calculations of V_{Ge}-rich environment. i is the index used in Table. 3.2.

doi:10.6342/NTU201701378

the total energy. Nevertheless, this merely indicates that when there are many V_{Ge}, they will probably favor staying close by rather than on the opposite sides of S_{Sb}.

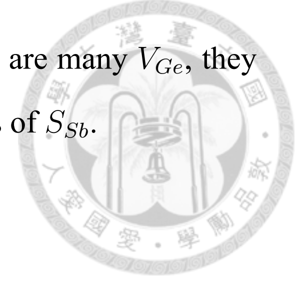

3.3.4 Summary of the energetics

From the results presented in previous sections, we have found that V_{Ge} and S_{Sb} facilitate the formation of each other in the GeTe system based on an energy point of view. This addresses the question why GST compounds are often reported with large concentration of V_{Ge} [18,28,45,48].

3.4 Structural relaxation

Here we investigate the crystal structure relaxation induced by inserting defects. A $4 \times 4 \times 4$ SC is adopted in the calculation. Similar to Fig. 3.1, for visualization, the purple balls and the yellow balls are used to represent Ge atoms and Te atoms, respectively. Additionally, V_{Ge} are represented by black balls, and S_{Sb} are represented by orange balls. Except for the site at the center, each Ge atom is attached with a red arrow, and each Te atom is attached with a green arrow. The arrows indicate the magnitude and direction of the displacement of each atom after adding the defects. For visual convenience,the scale of the arrow length is different in each figure. To simplify the figures, we will show only the first and second nearest layers of Ge and Te with respect to the defect at the center.

3.4.1 Single defect induced relaxation

Relaxations of two $4 \times 4 \times 4$ SCs each containing a V_{Ge} (type-V_{Ge}) or S_{Sb} (type-S_{Sb}) are calculated. The results are illustrated in Fig. 3.5.

It is obvious that in both relaxation types, the induced displacement is significant only for the atoms on the Cartesian x-, y-, and z-axis, while it is negligible for other atoms. We thus explicitly extract the data of those atoms, including the first nearest Te layer (denoted by $\mathrm{NL}^1_{\mathrm{Te}}$) and the second nearest Ge layer (denoted by $\mathrm{NL}^2_{\mathrm{Ge}}$), into Table. 3.3. The largest induced atomic displacement in the presence of V_{Ge} is 0.154 Å, which is consistent to the

doi:10.6342/NTU201701378

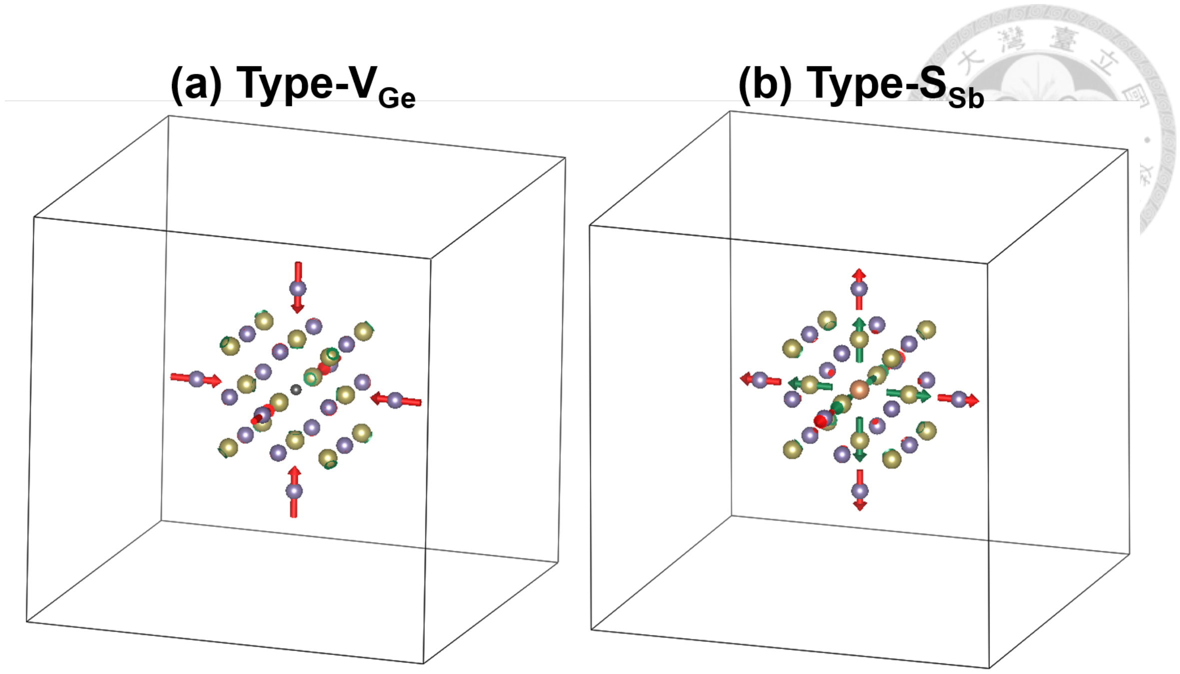

Figure 3.5: Structural relaxation of a $4 \times 4 \times 4$ SC in the presence of **(a)** a single V_{Ge} (black ball) at the center, and **(b)** a single S_{Sb} (orange ball) at the center.

result given by Edwards *et al.* [11]

Table 3.3: Displacement data for the atoms on Cartesian axes in Fig. 3.5.

	(a) Type-V_{Ge}	(b) Type-S_{Sb}
$\mathrm{NL}^1_{\mathrm{Te}}$	0.002 Å outward	0.067 Å outward
$\mathrm{NL}^2_{\mathrm{Ge}}$	0.154 Å inward	0.061 Å outward

For the type-V_{Ge} relaxation, it is not surprising that $\mathrm{NL}^2_{\mathrm{Ge}}$ will move inward, since the removal of a Ge atom at the center will release considerable space. However, although being closer to the center, $\mathrm{NL}^1_{\mathrm{Te}}$ barely move. This may be due to the combination of geometric and chemical tendencies. Like $\mathrm{NL}^2_{\mathrm{Ge}}$, $\mathrm{NL}^1_{\mathrm{Te}}$ also tends to move inward in response to the released space. Nevertheless, due to their anion role in GeTe system, Te atoms tend to grab electrons from Ge atoms. Since a Ge atom is now removed, the surrounding Te atoms move away from the vacancy in order to seek compensation from the Ge atoms on the opposite sides. These two kinds of tendency cancel out, which leads to the steadiness of $\mathrm{NL}^1_{\mathrm{Te}}$.

For the type-S_{Sb} relaxation, the mechanism is rather straightforward. Since the sub-

doi:10.6342/NTU201701378

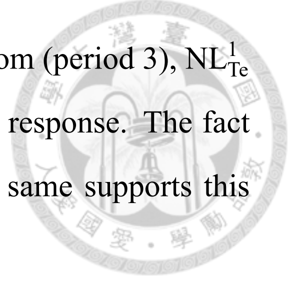

stitutional Sb atom (period 4) is bigger in size than the original Ge atom (period 3), NL^1_{Te} is pushed outward, and NL^2_{Ge} moves outward as well as a secondary response. The fact that the displacement magnitudes of NL^1_{Te} and NL^2_{Ge} are nearly the same supports this explanation.

3.4.2 Relaxation induced by the combination of V_{Ge} and S_{Sb}

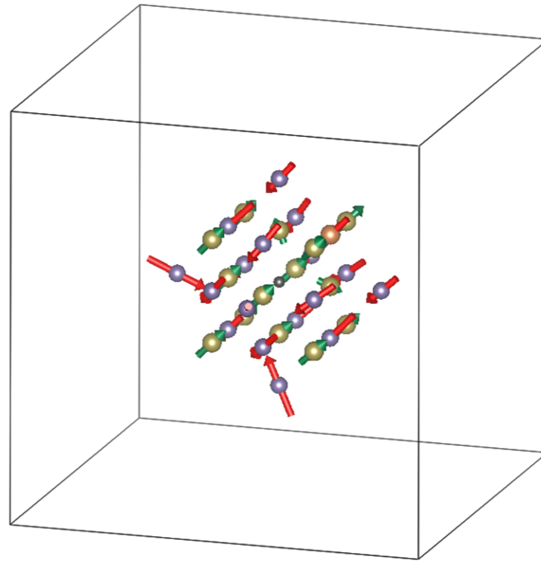

Figure 3.6: Structural relaxation of a $4 \times 4 \times 4$ SC in the presence of a V_{Ge} and a S_{Sb}.

For further verification, we also calculated the relaxation of a $4 \times 4 \times 4$ SC containing both a V_{Ge} and a S_{Sb} as illustrated in Fig. 3.6. The two defects are arranged as nearest neighbors on the Ge-sublattice. The displacement magnitudes of the atoms are confirmed all smaller than 0.2 Å.

3.4.3 Summary of relaxation analysis

It has been shown that the relaxation induced by V_{Ge} and S_{Sb} in GeTe systems is fairly small. Furthermore, if the defects are disordered as described in Ref. [7, 8, 26–28, 39, 42], the relaxation is likely to average out. Not only does this suggest that doping Sb into GeTe will not change the crystal structure, but it supports the fact that the cubic structure of GST samples can sustain very large concentration of vacancies [18, 28, 45, 48].

doi:10.6342/NTU201701378

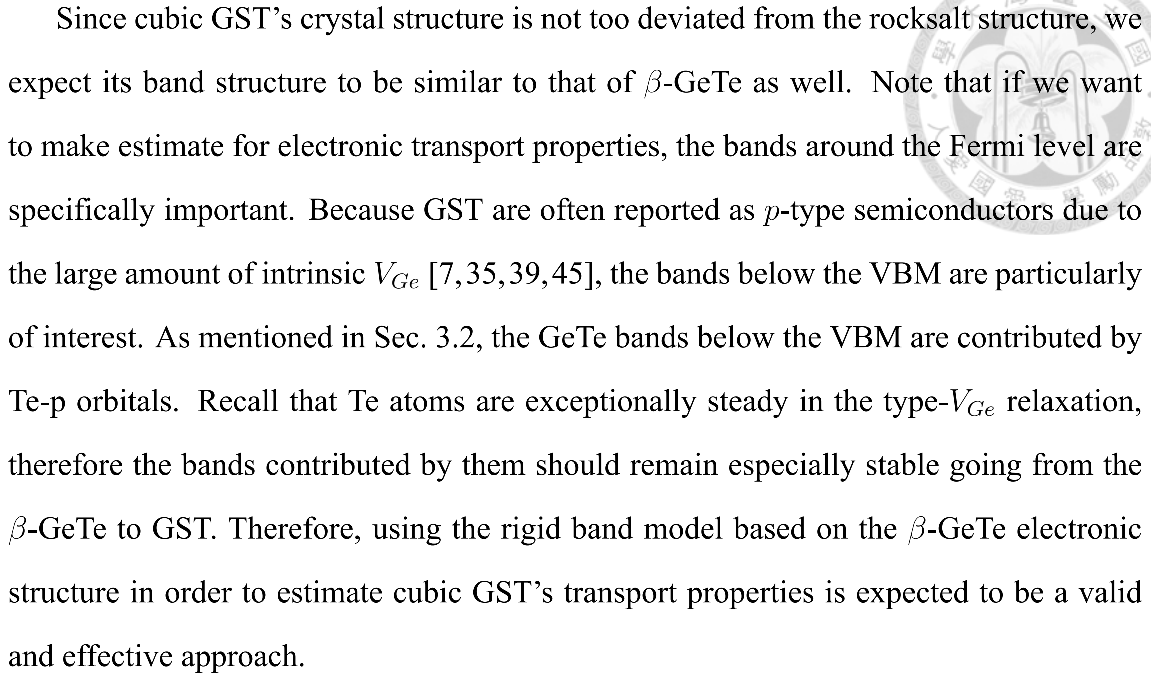

Since cubic GST's crystal structure is not too deviated from the rocksalt structure, we expect its band structure to be similar to that of β-GeTe as well. Note that if we want to make estimate for electronic transport properties, the bands around the Fermi level are specifically important. Because GST are often reported as p-type semiconductors due to the large amount of intrinsic V_{Ge} [7,35,39,45], the bands below the VBM are particularly of interest. As mentioned in Sec. 3.2, the GeTe bands below the VBM are contributed by Te-p orbitals. Recall that Te atoms are exceptionally steady in the type-V_{Ge} relaxation, therefore the bands contributed by them should remain especially stable going from the β-GeTe to GST. Therefore, using the rigid band model based on the β-GeTe electronic structure in order to estimate cubic GST's transport properties is expected to be a valid and effective approach.

3.5 Unfolded band structures

In this section, we investigate explicitly how the band structure is going to be affected by various concentrations of defects. SC with various sizes are constructed and inserted with a few defects. After being fully relaxed, their unfolded band structures are then obtained by using the BandUP [29] code. As for band structure plots, the PC k-path along which the unfolded bands are drawn is identical to the one used in Fig. 3.2, and the Fermi level in each graph is set to be zero.

3.5.1 Electron counting

Some prior knowledge regarding the relation between the composition, number of electrons, and electronic states could be helpful for understanding the position of the Fermi levels in the figures that we are going to discuss.

To begin with, any SC that we calculate corresponds to a normalized chemical formula:

$$\mathrm{Ge}_{(1-\mathrm{C_V}-\mathrm{C_S})}\mathrm{Sb}_{(\mathrm{C_S})}\mathrm{Te}, \tag{3.1}$$

where $\mathrm{C_V}$ is the concentration of V_{Ge}, and $\mathrm{C_S}$ is the concentration of S_{Sb}. Then, according

doi:10.6342/NTU201701378

to the valence electrons of each atom given in A.2, the normalized total number of valence electrons used in the DFT calculation is equal to

$$N = 10 - 4C_V + 1C_S. \tag{3.2}$$

Also, we have found that regardless of which SC we use, the integrated number of states at VBM will always follow

$$IDOS\Big|_{VBM} = 10 - 2C_V. \tag{3.3}$$

Eq. 3.3 suggests that the states below VBM is independent of the presence of S_{Sb}. This is not surprising, since the states below VBM originally provided by Ge atoms can be fully compensated by the states of Sb atoms.

Using Eq. 3.1, 3.2, and 3.3, we can thus have a sense of the position of the Fermi level of each SC.

3.5.2 Band structure with defects

Here we consider the unfolded bands from SC calculations with different sizes where each contains one V_{Ge} or one S_{Sb}. The SC used and their corresponding normalized chemical formula and defect concentrations are listed in A.3. The smaller the SC is, the larger the defect concentration it has.

The result for the SC containing one V_{Ge} is shown in Fig. 3.7. As described by Eq. 3.3 and 3.2, we simultaneously lose 4 electrons and 1 state below VBM whenever a V_{Ge} is formed. Since the loss of state cannot compensate the loss of electrons, the Fermi level is lowered into the valence band. On the other hand, the result for the SC containing S_{Sb} is given in Fig. 3.8. On the contrary, in these cases the Fermi level moves into the conduction band due to the extra electrons provided by Sb. Clearly, for all the cases considered above, the region near the VBM barely reveals new features, and the overall dispersions remain very similar to the β-GeTe band structure up to 12 at.% of defect.

doi:10.6342/NTU201701378

Figure 3.7: Unfolded bands for **(a)** 3×3×3 SC **(b)** 2×3×3 SC **(c)** 2×2×3 SC **(d)** 2×2×2 SC, each containing one V_{Ge}.

doi:10.6342/NTU201701378

Figure 3.8: Unfolded bands for **(a)** 3×3×3 SC **(b)** 2×3×3 SC **(c)** 2×2×3 SC **(d)** 2×2×2 SC, each containing one S_{Sb}.

doi:10.6342/NTU201701378

3.5.3 Band structure with both V_{Ge} and S_{Sb}

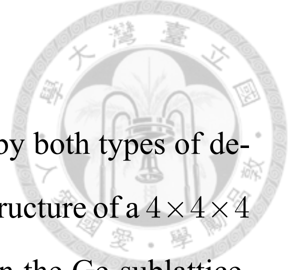

For further confirmation, we investigate the combined influence by both types of defects on the band structure. Note that in Ref. [45], the unfolded band structure of a $4\times4\times4$ SC containing a V_{Ge} and a S_{Sb}, arranged as first nearest neighbors on the Ge-sublattice, is already shown very similar to the β-GeTe band structure. Here, we want to consider a SC containing two V_{Ge} and one S_{Sb}, which was previously discussed in Sec. 3.3.3. Since $2V_{Ge}^1$ is shown to have the lowest total energy among all possible configurations listed in Table 3.2, it is chosen as our SC here. The unfolded bands of $2V_{Ge}^1$ is shown in Fig. 3.9**(a)**.

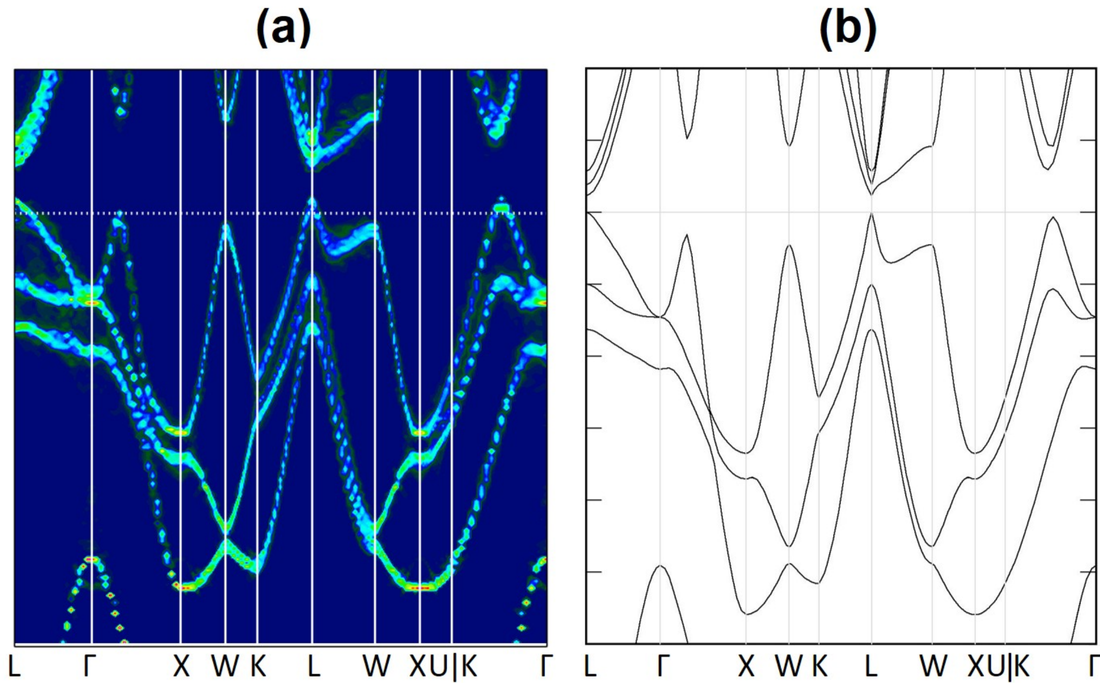

Figure 3.9: **(a)** Unfolded bands of the $2V_{Ge}^1$ SC from Table 3.2. **(b)** Zoom-in band structure of β-GeTe for comparison.

In this case, the defect concentration is 4.7at.% (3.1 at.% of V_{Ge}, 1.6 at.% of S_{Sb}). It is obvious from Eq. 3.2 and 3.3 that in this configuration, the system exhibits a p-type behavior with its Fermi level below the VBM. The dispersions are again very similar to those of β-GeTe. Although there are some splittings near -5 eV, they are too deep and is irrelevant to transport properties. However, it is noteworthy that there is also a minor splitting of about 0.3 eV at the W-point near -0.5 eV. This splitting gives an estimate of

doi:10.6342/NTU201701378

the error bar that we may have if we are to calculate the transport properties of cubic GST using β-GeTe band structure.

3.5.4 Quantitative measure of band rigidity

To obtain a quantitative measure of the rigidities of SC electronic structures, we compute the "root-mean-square deviation (RMSD) per energy eigenvalue" of the unfolded spectra by comparing them to the PC spectrum. In order to do this, a Γ-centered $4 \times 4 \times 4$ Monkhorst-Pack k-mesh is adopted to calculate the PC spectrum, and the SC electronic structures are unfolded onto this k-mesh, subsequently. Here, only the states below the VBM are considered. And for the purpose of reducing numerical noise, in each unfolded spectra, the spectral points with intensities smaller than 9% of the maximum intensity are dropped. Then, using the bottom of valence band as the reference point for alignments, we assign each of the remainder spectral peaks to its closest energy eigenvalue in PC spectrum and calculate the distance between them. Lastly, with proper weighting and averaging, we derive the RMSD per energy eigenvalue for each SC's unfolded spectrum. From the fact that the bottom s-bands, as shown in Fig. 3.2, are irrelevant to the transport properties and are completely separated from other bands, we also compute the RMSD per energy eigenvalue solely for the p-bands near the VBM by excluding the contribution by the s-bands. Since Fig. 3.7(d), 3.8(d), and 3.9(a) are the most representative unfolded band structures for they have the largest concentration of defects or show the combined influence by both types of defects, we only calculate the RMSD per energy eigenvalue for the SCs corresponding to these figures. The results for the three unfolded spectra are listed in Table. 3.4. As we can see, the deviation per energy eigenvalue, which gives an estimate of the error bar that we may have when calculating transport properties, is less than a small value of 0.2 eV.

3.5.5 Summary of unfolded bands

It has been explicitly shown that the band structure of β-GeTe is barely affected by the presence of either V_{Ge}, S_{Sb}, or a combination of them up to large concentrations. This

doi:10.6342/NTU201701378

Table 3.4: Root-mean-square deviation per energy eigenvalue for the unfolded spectra. The unit is in eV.

Corresponding supercell	s-bands included	s-bands excluded
Fig. 3.7(d) $2 \times 2 \times 2$ w/ $1V_{Ge}$	0.187	0.175
Fig. 3.8(d) $2 \times 2 \times 2$ w/ $1S_{Sb}$	0.111	0.081
Fig. 3.9(a) $4 \times 4 \times 4$ w/ $2V_{Ge}$ & $1S_{Sb}$	0.108	0.118

agrees with the prediction from the structural analyses in Sec. 3.4.

Moreover, if we set VBM as reference point (E $= 0$), the Fermi level and the number of electrons per normalized chemical formula (Eq. 3.2) of each SC will strictly follow a linear relation, as shown in Fig. 3.10.

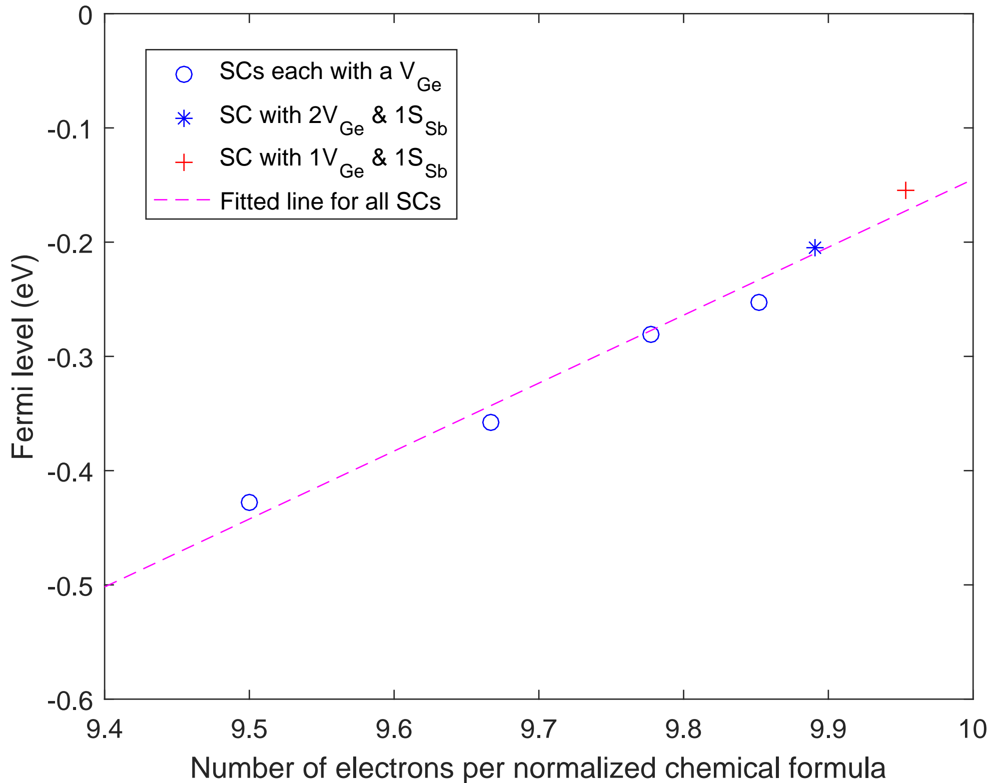

Figure 3.10: Fermi level versus number of electrons per chemical formula of each SC.

These evidences suggest that the effect of adding V_{Ge} and S_{Sb} into GST system is actually just tuning the Fermi level of the system. Therefore, the validity of the rigid band model of using β-GeTe electronic structure to estimate cubic GST's transport properties

doi:10.6342/NTU201701378

is again verified.

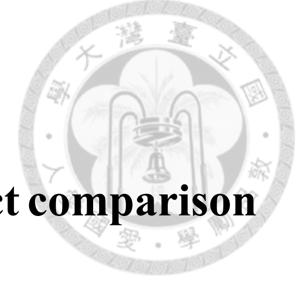

3.6 Boltzmann theory calculations and direct comparison to experiment data

In the previous sections, the rigid band model approach of using the β-GeTe electronic structure to estimate cubic GST's transport properties has been shown to be promising. In this section, we test the applicability of the approach by directly comparing the experimentally measured transport data to our Boltzmann theory calculations done by the BoltzTraP [25] code.

Since the GST thin films reported by Wong *et al*. [45] possess so far the best thermoelectric performance, we choose them as our subject of comparison.

3.6.1 Experimental results by Wong *et al.* [45]

We now introduce some information regarding the GST thin films that we will make comparisons with. They are prepared on Si substrates, and are shown to be in the $Fm\bar{3}m$ cubic rocksalt phase throughout the operating temperature range of 25–300°C. They are reported with an extreme stoichiometry of $Ge_{0.566}Sb_{0.171}Te$ with up to 25 at.% vacancies, which can be explained by our energetics calculations in Sec. 3.3 and structural relaxation calculations in Sec. 3.4. Using the VBM as the reference point ($E = 0$), ultraviolet photoelectron spectroscopy (UPS) data show that their Fermi level decreases from -0.24 to -0.52 eV with respect to the increase in temperature. Accordingly, we begin our calculation by scanning the Fermi level from -0.1 eV to -0.5 eV on the β-GeTe band structure with an energy step of 0.1 eV. The positions of the scanned levels are illustrated in A.4. For more details regarding the GST thin films, one can refer to Ref. [45].

doi:10.6342/NTU201701378

3.6.2 Seebeck coefficient

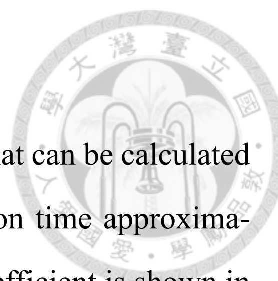

As explained in Section 2.3, Seebeck coefficients are quantities that can be calculated without ambiguity in Boltzmann theory under the constant relaxation time approximation. The comparison of the computed and the measured Seebeck coefficient is shown in Fig. 3.11. Clearly, the Fermi level at -0.1 eV gives a very accurate estimation.

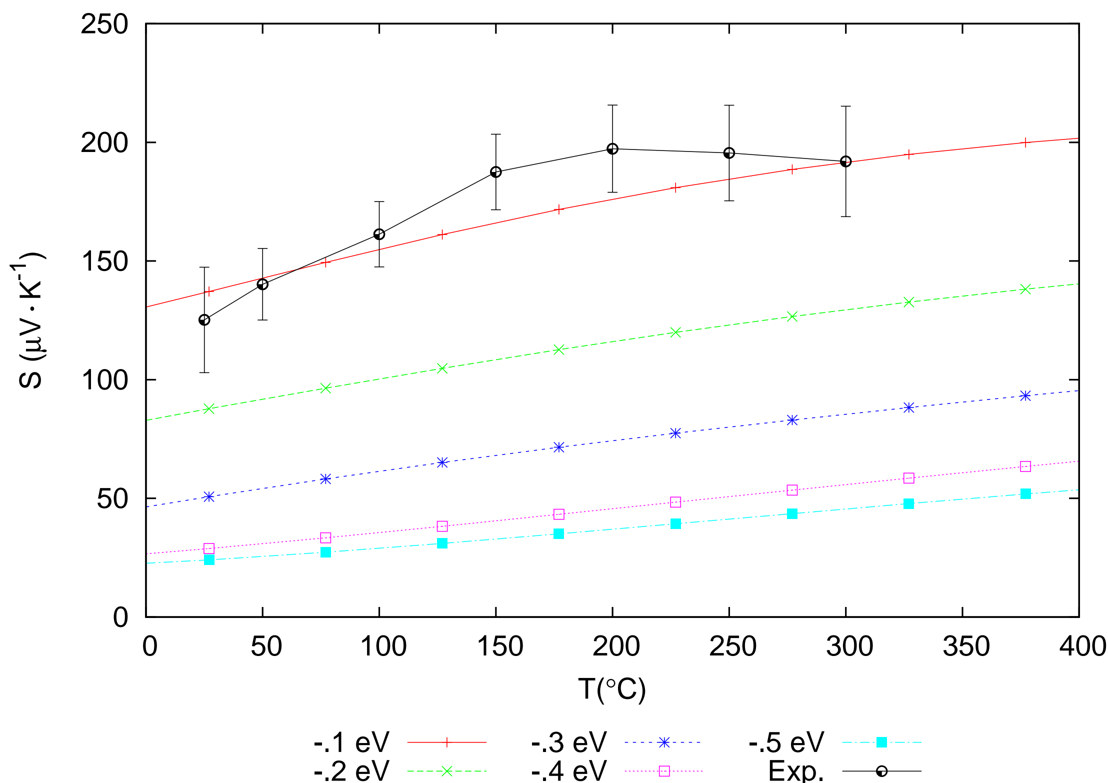

Figure 3.11: Seebeck coefficient as a function of temperature. “Exp.” is the measured Seebeck coefficient of the GST thin flims provided by Wong *et al.* [45]

3.6.3 Carrier concentration

Carrier concentration is another quantity that can be obtained without ambiguity. The comparison of the computed and the measured carrier concentration is shown in Fig. 3.11. The experimental result of the carrier concentration shows a significant increase with temperature. Wong *et al.* attribute this to the decrease of Fermi level into deeper bands [45]. Here, by directly comparing the computed curves and the measured curve, it is shown that the Fermi level should drop from -0.1 eV to -0.4 eV with temperature. This agrees with

doi:10.6342/NTU201701378

the observed amount of decrement of the Fermi level, and the errorbar of Fermi level we predicted in Sec. 3.5.3.

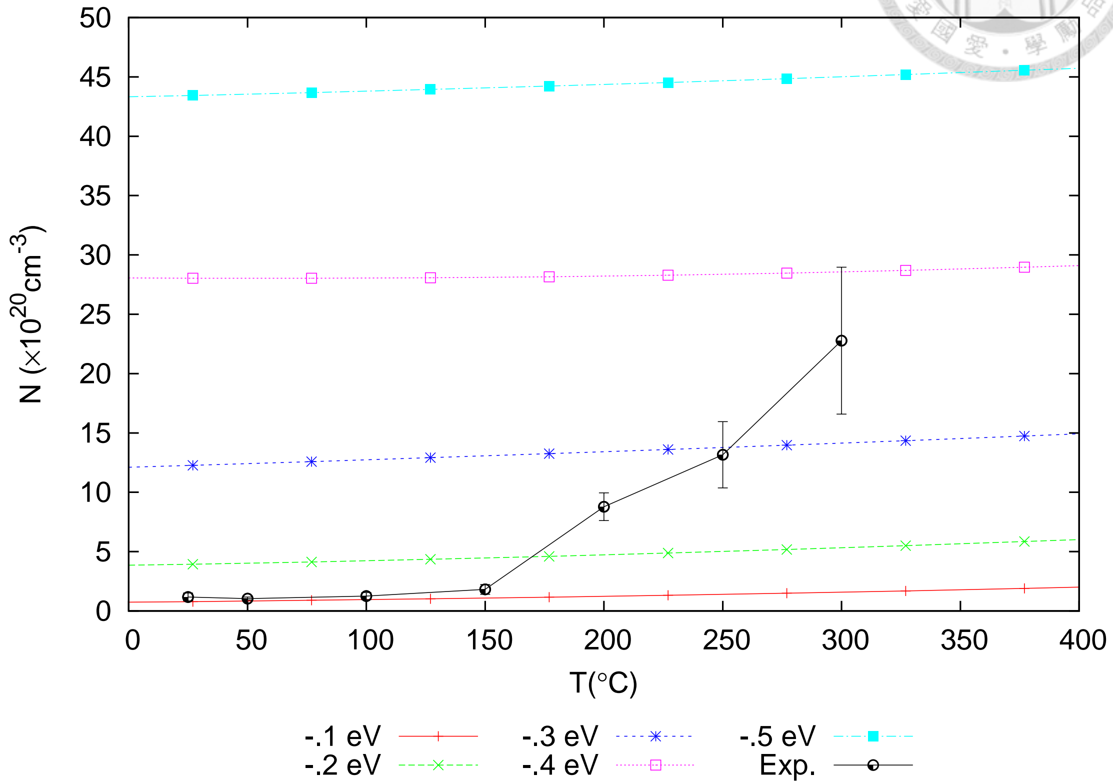

Figure 3.12: Carrier concentration versus temperature. "Exp." is the measured carrier concentration of the GST thin flims provided by Wong *et al.* [45]

3.6.4 Relaxation time

As described in Sec. 2.3, under the constant relaxation time approximation for Boltzmann theory, electrical conductivity and electronic thermal conductivity are inevitably derived with an relaxation time factor. This forbids us from directly comparing the computed data to the experimental data. However, we can estimate the relaxation time *twice* by comparing both the computed electrical conductivity and electronic thermal conductivity to the experiment results, and check if the two values derived individually are consistent.

The calculated electrical conductivity over the relaxation time (σ/τ) and the measured electrical conductivity of the GST thin films are plotted in Fig. 3.13. As shown in the figure, the observed electrical conductivity is ~10^5 $\Omega^{-1}m^{-1}$. If we believe that the

doi:10.6342/NTU201701378

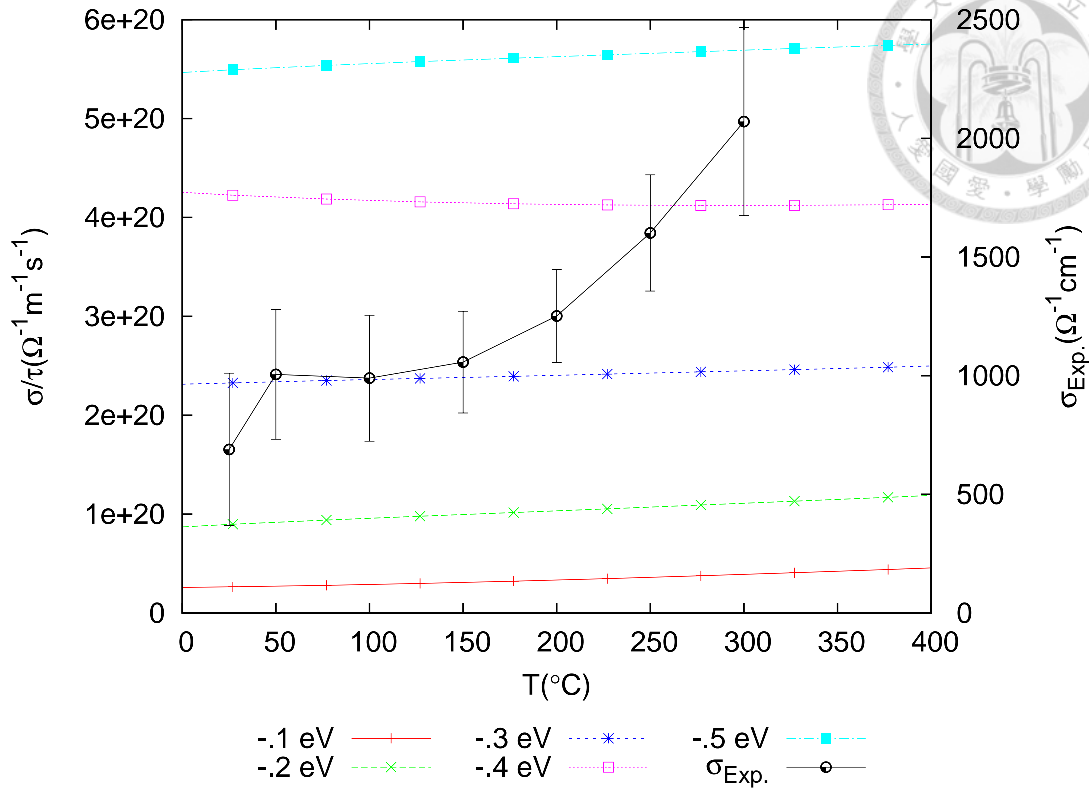

Figure 3.13: The curves labelled with “eV” are the calculated electrical conductivity over relaxation time (σ/τ). “$\sigma_{\text{Exp.}}$” is the data of the measured electrical conductivity of the GST films provided by Wong *et al.* [45]

Fermi level really does lie in the range in which we do the calculation (-0.1 to -0.5 eV), the computed σ/τ is ~10^{20} $\Omega^{-1}m^{-1}s^{-1}$. This means that the relaxation time should be ~10^{-15} s.

The calculated electronic thermal conductivity over the relaxation time (κ_{ele}/τ) and the measured *total* thermal conductivity of the GST thin films are plotted in Fig. 3.14. The computed κ_{ele}/τ is ~10^{15} $W^{-1}m^{-1}K^{-1}s^{-1}$, the observed total thermal conductivity is ~10^{0} $W^{-1}m^{-1}K^{-1}$. Here we cannot extract the electronic contribution to the total thermal conductivity. However, if we assume that the electronic thermal conductivity is approximately of the same order of magnitude of the total thermal conductivity, then the relaxation time should be ~10^{-15} s, which is consistent with the estimation from electrical conductivity comparison.

doi:10.6342/NTU201701378

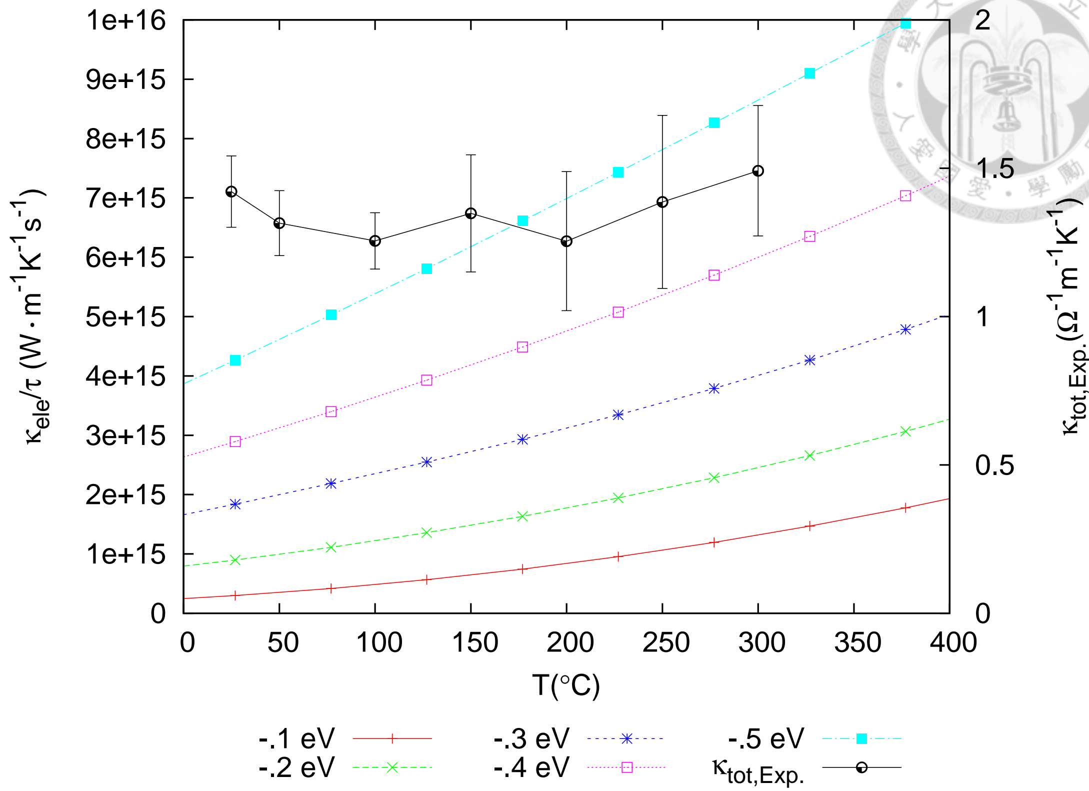

Figure 3.14: The curves labelled with "eV" are the computed electronic thermal conductivity over relaxation time (κ_{ele}/τ). "$\kappa_{\text{tot,Exp.}}$" is the data of the measured total conductivity of the GST films provided by Wong *et al.* [45].

3.6.5 Summary of transport calculations and speculation on the substrate

We have demonstrated that by using the β-GeTe band structure, we can make reasonable estimates of the transport properties of the cubic GST systems. Furthermore, by comparing to the experimental transport data, our rigid band model predicts a Fermi level of the GST thin films to lie between -0.1 to -0.5 eV below VBM, which is in good agreement with -0.24 to -0.52 eV observed by the UPS measurement [45].

However, using Eq. 3.2 and the composition mentioned in Sec. 3.6.1, the number of electrons per normalized chemical formula of the GST thin films should be 9.12. If the linear relation between the number of electrons and the depth of chemical potential in Fig. 3.10 is correct, then the GST thin films should have their Fermi level much lower than -0.5 eV, which disagrees with both the experiment measurement and our calculation.

doi:10.6342/NTU201701378

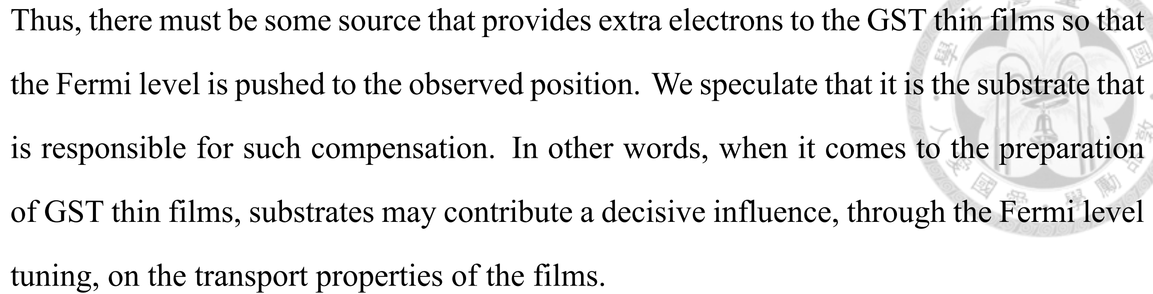

Thus, there must be some source that provides extra electrons to the GST thin films so that the Fermi level is pushed to the observed position. We speculate that it is the substrate that is responsible for such compensation. In other words, when it comes to the preparation of GST thin films, substrates may contribute a decisive influence, through the Fermi level tuning, on the transport properties of the films.

3.7 Conclusion

In this work, we have studied the cubic GST systems by comparing them to β-GeTe. Our energetics calculations showed that the Ge vacancies and Sb substitution facilitate the presence of each other in β-GeTe system, which explains the often reported extreme stoichiometries of cubic GST compounds. By investigating the deformation of the crystal structure and the band structure, we showed that the Ge vacancies and Sb substitutions barely perturb the cubic GST systems from β-GeTe characteristics. This indicates that the function of them is merely tunning the Fermi level. Based on these facts, we proposed a rigid band model of using the β-GeTe band structure to estimate the transport properties of cubic GST systems. By directly comparing with the experiment results of the GST thin films reported by Wong *et al*. [45], we demonstrated the accuracy and usefulness of the rigid band model. Additionally, we speculate that the substrate play an decisive role in the transport properties of cubic GST thin films.

GST is a very promising type of thermoelectric material because of its superior and tunable thermoelectric properties. We believe that our work will serve as a guideline that expedites the understanding, design, and engineering processes of GST for thermoelectric applications.

doi:10.6342/NTU201701378

Appendix A

A.1 High symmetry points

The k-points is defined as

$$\mathbf{k} = x_1\mathbf{b}_1 + x_2\mathbf{b}_2 + x_3\mathbf{b}_3,$$

where $\mathbf{b}_i$ are reciprocal lattice vectors of the rocksalt primitive cell. The x_i values of each high symmetry point used are listed below.

Points	x_1	x_2	x_3
Γ	0	0	0
L	0.5	0.5	0.5
X	0.5	0	0.5
W	0.5	0.25	0.75
K	0.375	0.375	0.75
U	0.625	0.25	0.625

doi:10.6342/NTU201701378

A.2 Valence electrons used in DFT calculation

The table below lists the valence electrons used for each type of atom in the DFT calculation as implemented in VASP [19, 20] code.

Atom	Period	Group	Valence electrons
Ge	4	III	s^2p^2
Sb	5	IV	s^2p^3
Te	5	V	s^2p^4

A.3 Supercells used in Sec. 3.5.2

The supercells (SCs) used in Sec. 3.5.2 and their corresponding normalized chemical formula and defect concentrations on the Ge-sublattice are listed in the following table.

SC	V_{Ge}	S_{Sb}	Defect cocentration
3×3×3	$Ge_{0.9630}Te$	$Ge_{0.9630}Sb_{0.0370}Te$	3.70 at.%
2×3×3	$Ge_{0.9444}Te$	$Ge_{0.9444}Sb_{0.0556}Te$	5.56 at.%
2×2×3	$Ge_{0.9167}Te$	$Ge_{0.9167}Sb_{0.0833}Te$	8.33 at.%
2×2×2	$Ge_{0.8750}Te$	$Ge_{0.8750}Sb_{0.1250}Te$	12.5 at.%

doi:10.6342/NTU201701378

A.4 Fermi level scanning

The levels in GeTe band structure for Fermi level scanning.

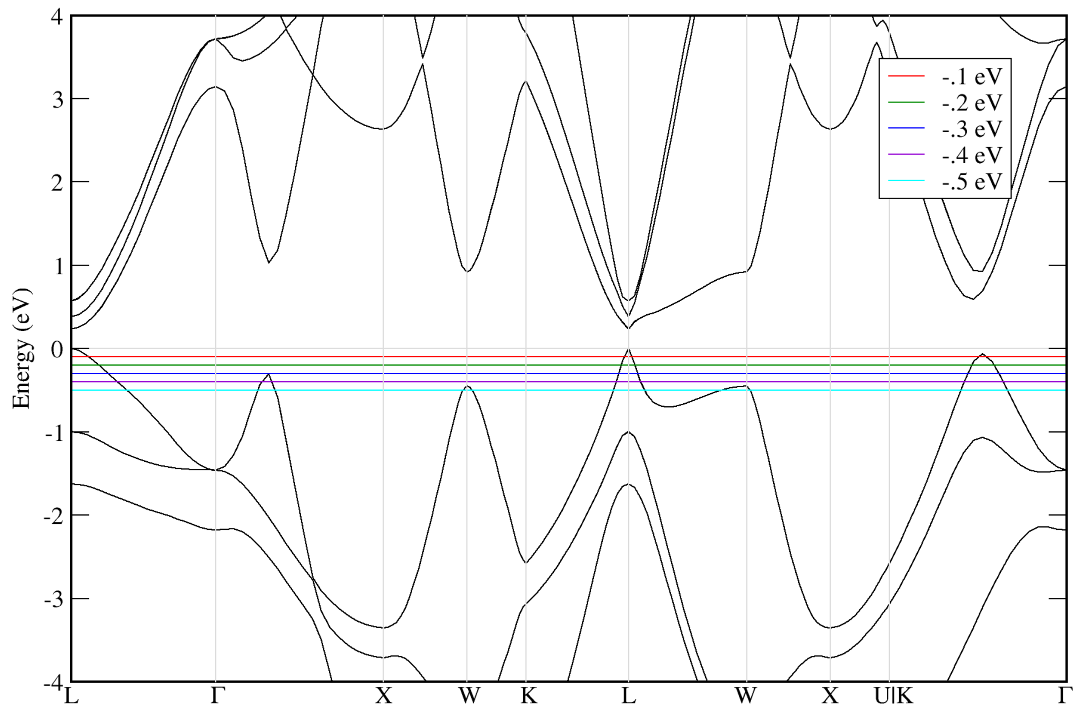

doi:10.6342/NTU201701378

Bibliography

[1] H. Alam and S. Ramakrishna. A review on the enhancement of figure of merit from bulk to nano-thermoelectric materials. Nano Energy, 2(2):190 – 212, 2013.

[2] N. Ashcroft and N. Mermin. Solid State Physics. Saunders College, Philadelphia, 1976.

[3] P. Bauer Pereira, I. Sergueev, S. Gorsse, J. Dadda, E. Müller, and R. P. Hermann. Lattice dynamics and structure of GeTe, SnTe and PbTe. physica status solidi (b), 250(7):1300–1307, 2013.

[4] L. E. Bell. Cooling, Heating, Generating Power, and Recovering Waste Heat with Thermoelectric Systems. Science, 321(5895):1457–1461, 2008.

[5] L. Bellaiche, S.-H. Wei, and A. Zunger. Composition dependence of interband transition intensities in GaPN, GaAsN, and GaPAs alloys. Phys. Rev. B, 56:10233–10240, Oct 1997.

[6] P. E. Blöchl. Projector augmented-wave method. Phys. Rev. B, 50:17953–17979, Dec 1994.

[7] I.-N. Chen, C.-W. Chong, D. P. Wong, L.-M. Lyu, W.-L. Chien, R. Anbalagan, M. Aminzare, Y.-F. Chen, L.-C. Chen, and K.-H. Chen. Improving the thermoelectric performance of metastable rock-salt GeTe-rich Ge−Sb−Te thin films through tuning of grain orientation and vacancies. physica status solidi (a), 213(12):3122–3129, 2016.

doi:10.6342/NTU201701378

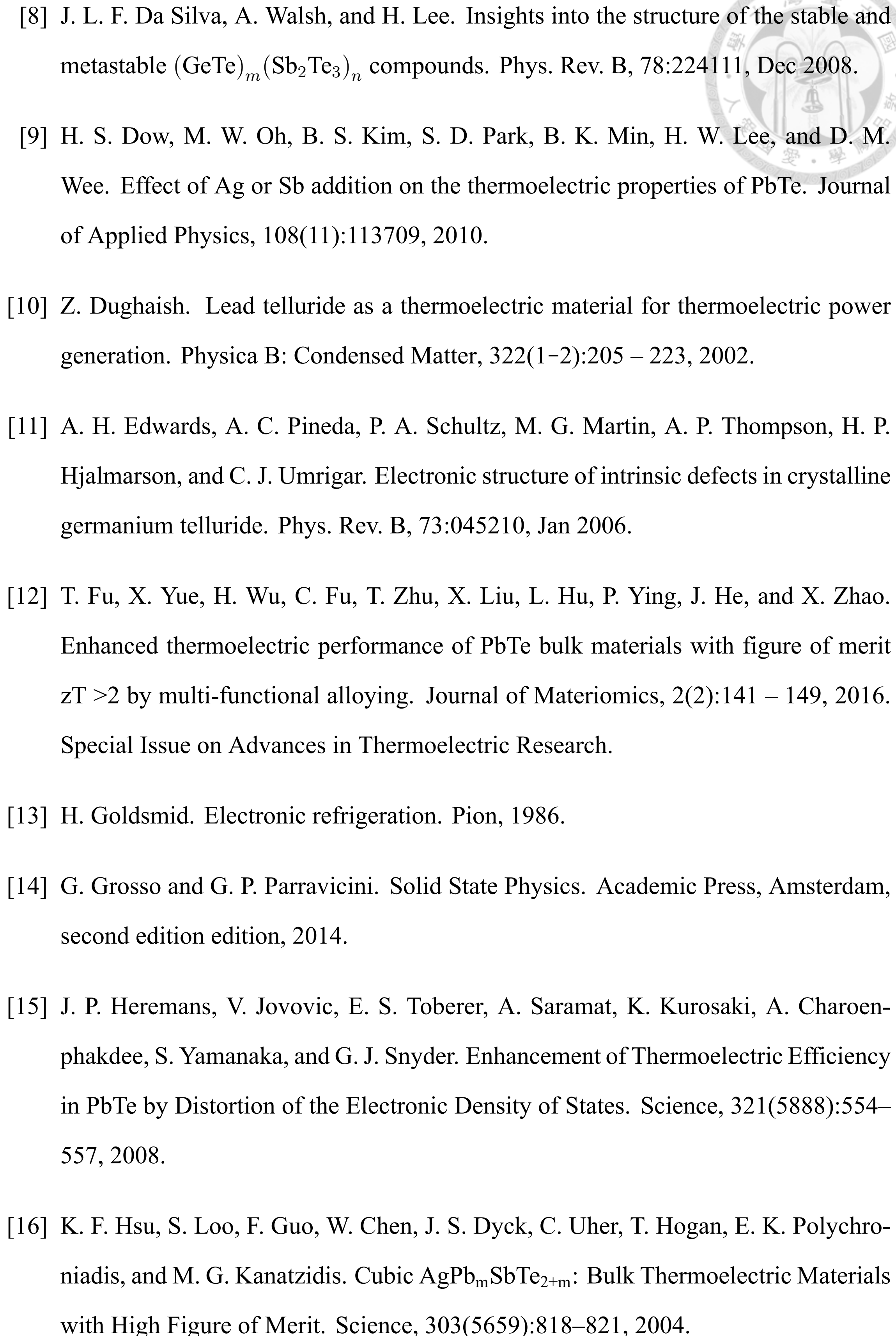

[8] J. L. F. Da Silva, A. Walsh, and H. Lee. Insights into the structure of the stable and metastable $(\mathrm{GeTe})_m(\mathrm{Sb_2Te_3})_n$ compounds. Phys. Rev. B, 78:224111, Dec 2008.

[9] H. S. Dow, M. W. Oh, B. S. Kim, S. D. Park, B. K. Min, H. W. Lee, and D. M. Wee. Effect of Ag or Sb addition on the thermoelectric properties of PbTe. Journal of Applied Physics, 108(11):113709, 2010.

[10] Z. Dughaish. Lead telluride as a thermoelectric material for thermoelectric power generation. Physica B: Condensed Matter, 322(1–2):205 – 223, 2002.

[11] A. H. Edwards, A. C. Pineda, P. A. Schultz, M. G. Martin, A. P. Thompson, H. P. Hjalmarson, and C. J. Umrigar. Electronic structure of intrinsic defects in crystalline germanium telluride. Phys. Rev. B, 73:045210, Jan 2006.

[12] T. Fu, X. Yue, H. Wu, C. Fu, T. Zhu, X. Liu, L. Hu, P. Ying, J. He, and X. Zhao. Enhanced thermoelectric performance of PbTe bulk materials with figure of merit zT >2 by multi-functional alloying. Journal of Materiomics, 2(2):141 – 149, 2016. Special Issue on Advances in Thermoelectric Research.

[13] H. Goldsmid. Electronic refrigeration. Pion, 1986.

[14] G. Grosso and G. P. Parravicini. Solid State Physics. Academic Press, Amsterdam, second edition edition, 2014.

[15] J. P. Heremans, V. Jovovic, E. S. Toberer, A. Saramat, K. Kurosaki, A. Charoenphakdee, S. Yamanaka, and G. J. Snyder. Enhancement of Thermoelectric Efficiency in PbTe by Distortion of the Electronic Density of States. Science, 321(5888):554–557, 2008.

[16] K. F. Hsu, S. Loo, F. Guo, W. Chen, J. S. Dyck, C. Uher, T. Hogan, E. K. Polychroniadis, and M. G. Kanatzidis. Cubic $\mathrm{AgPb_mSbTe_{2+m}}$: Bulk Thermoelectric Materials with High Figure of Merit. Science, 303(5659):818–821, 2004.

doi:10.6342/NTU201701378

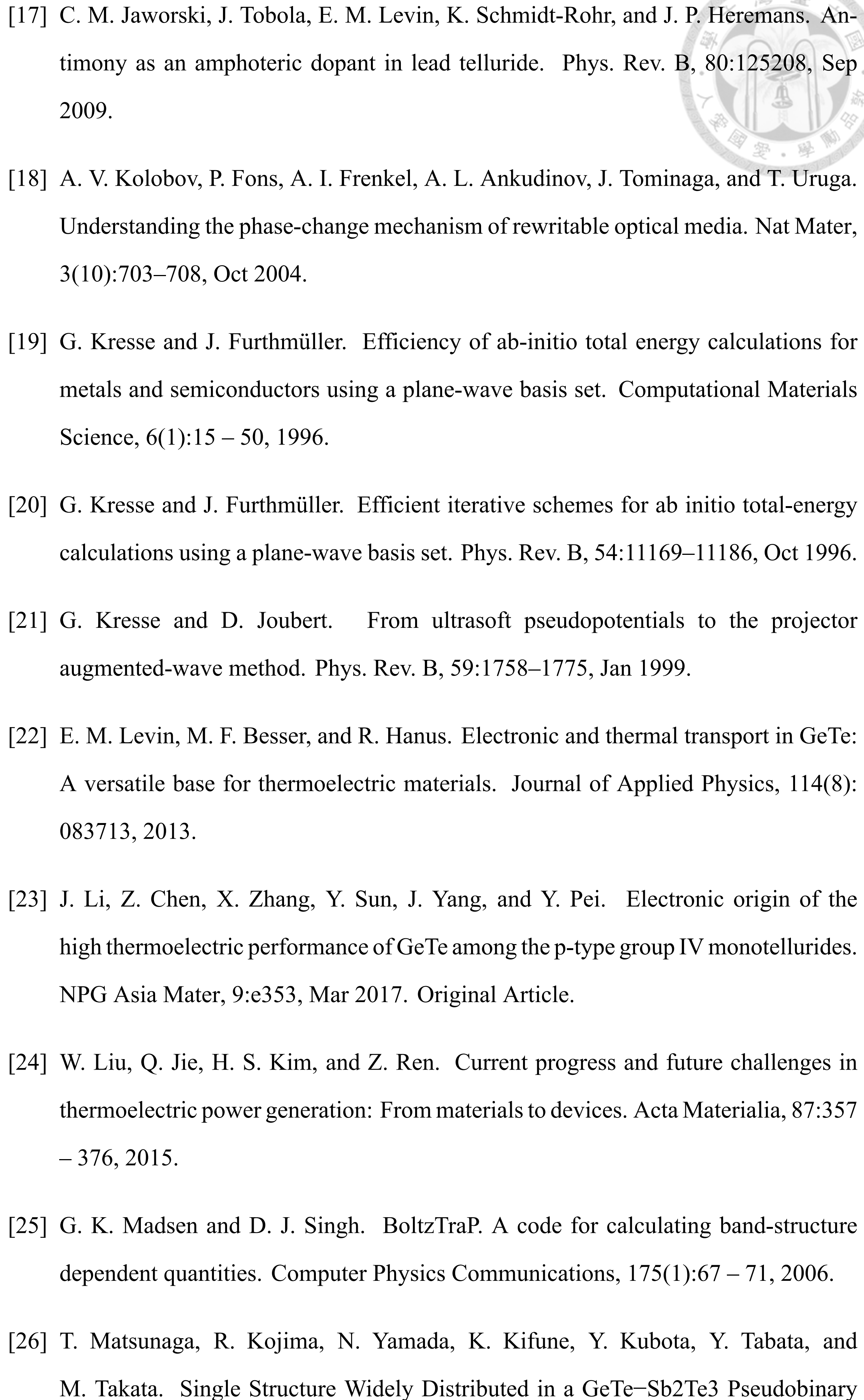

[17] C. M. Jaworski, J. Tobola, E. M. Levin, K. Schmidt-Rohr, and J. P. Heremans. Antimony as an amphoteric dopant in lead telluride. Phys. Rev. B, 80:125208, Sep 2009.

[18] A. V. Kolobov, P. Fons, A. I. Frenkel, A. L. Ankudinov, J. Tominaga, and T. Uruga. Understanding the phase-change mechanism of rewritable optical media. Nat Mater, 3(10):703–708, Oct 2004.

[19] G. Kresse and J. Furthmüller. Efficiency of ab-initio total energy calculations for metals and semiconductors using a plane-wave basis set. Computational Materials Science, 6(1):15 – 50, 1996.

[20] G. Kresse and J. Furthmüller. Efficient iterative schemes for ab initio total-energy calculations using a plane-wave basis set. Phys. Rev. B, 54:11169–11186, Oct 1996.

[21] G. Kresse and D. Joubert. From ultrasoft pseudopotentials to the projector augmented-wave method. Phys. Rev. B, 59:1758–1775, Jan 1999.

[22] E. M. Levin, M. F. Besser, and R. Hanus. Electronic and thermal transport in GeTe: A versatile base for thermoelectric materials. Journal of Applied Physics, 114(8): 083713, 2013.

[23] J. Li, Z. Chen, X. Zhang, Y. Sun, J. Yang, and Y. Pei. Electronic origin of the high thermoelectric performance of GeTe among the p-type group IV monotellurides. NPG Asia Mater, 9:e353, Mar 2017. Original Article.

[24] W. Liu, Q. Jie, H. S. Kim, and Z. Ren. Current progress and future challenges in thermoelectric power generation: From materials to devices. Acta Materialia, 87:357 – 376, 2015.

[25] G. K. Madsen and D. J. Singh. BoltzTraP. A code for calculating band-structure dependent quantities. Computer Physics Communications, 175(1):67 – 71, 2006.

[26] T. Matsunaga, R. Kojima, N. Yamada, K. Kifune, Y. Kubota, Y. Tabata, and M. Takata. Single Structure Widely Distributed in a GeTe−Sb2Te3 Pseudobinary

doi:10.6342/NTU201701378

System: A Rock Salt Structure is Retained by Intrinsically Containing an Enormous Number of Vacancies within its Crystal. Inorganic Chemistry, 45(5):2235–2241, 2006. PMID: 16499389.

[27] T. Matsunaga, H. Morita, R. Kojima, N. Yamada, K. Kifune, Y. Kubota, Y. Tabata, J.-J. Kim, M. Kobata, E. Ikenaga, and K. Kobayashi. Structural characteristics of GeTe-rich GeTe–Sb2Te3 pseudobinary metastable crystals. Journal of Applied Physics, 103(9):093511, 2008.

[28] T. Matsunaga and N. Yamada. Structural investigation of $GeSb_2Te_4$: A high-speed phase-change material. Phys. Rev. B, 69:104111, Mar 2004.

[29] P. V. C. Medeiros, S. Stafström, and J. Björk. Effects of extrinsic and intrinsic perturbations on the electronic structure of graphene: Retaining an effective primitive cell band structure by band unfolding. Phys. Rev. B, 89:041407, Jan 2014.

[30] G. Min and D. M. Rowe. Thermoelectric figure-of-merit barrier at minimum lattice thermal conductivity? Applied Physics Letters, 77(6):860–862, 2000.

[31] C. M. I. Okoye. Electronic and optical properties of SnTe and GeTe. Journal of Physics: Condensed Matter, 14(36):8625, 2002.

[32] Y. Pei, A. LaLonde, S. Iwanaga, and G. J. Snyder. High thermoelectric figure of merit in heavy hole dominated PbTe. Energy Environ. Sci., 4:2085–2089, 2011.

[33] Y. Pei, X. Shi, A. LaLonde, H. Wang, L. Chen, and G. J. Snyder. Convergence of electronic bands for high performance bulk thermoelectrics. Nature, 473(7345): 66–69, May 2011.

[34] J. P. Perdew and Y. Wang. Accurate and simple analytic representation of the electron-gas correlation energy. Phys. Rev. B, 45:13244–13249, Jun 1992.

[35] S. Perumal, S. Roychowdhury, D. S. Negi, R. Datta, and K. Biswas. High Thermoelectric Performance and Enhanced Mechanical Stability of p-type $Ge_{1-x}Sb_xTe$. Chemistry of Materials, 27(20):7171–7178, 2015.

doi:10.6342/NTU201701378

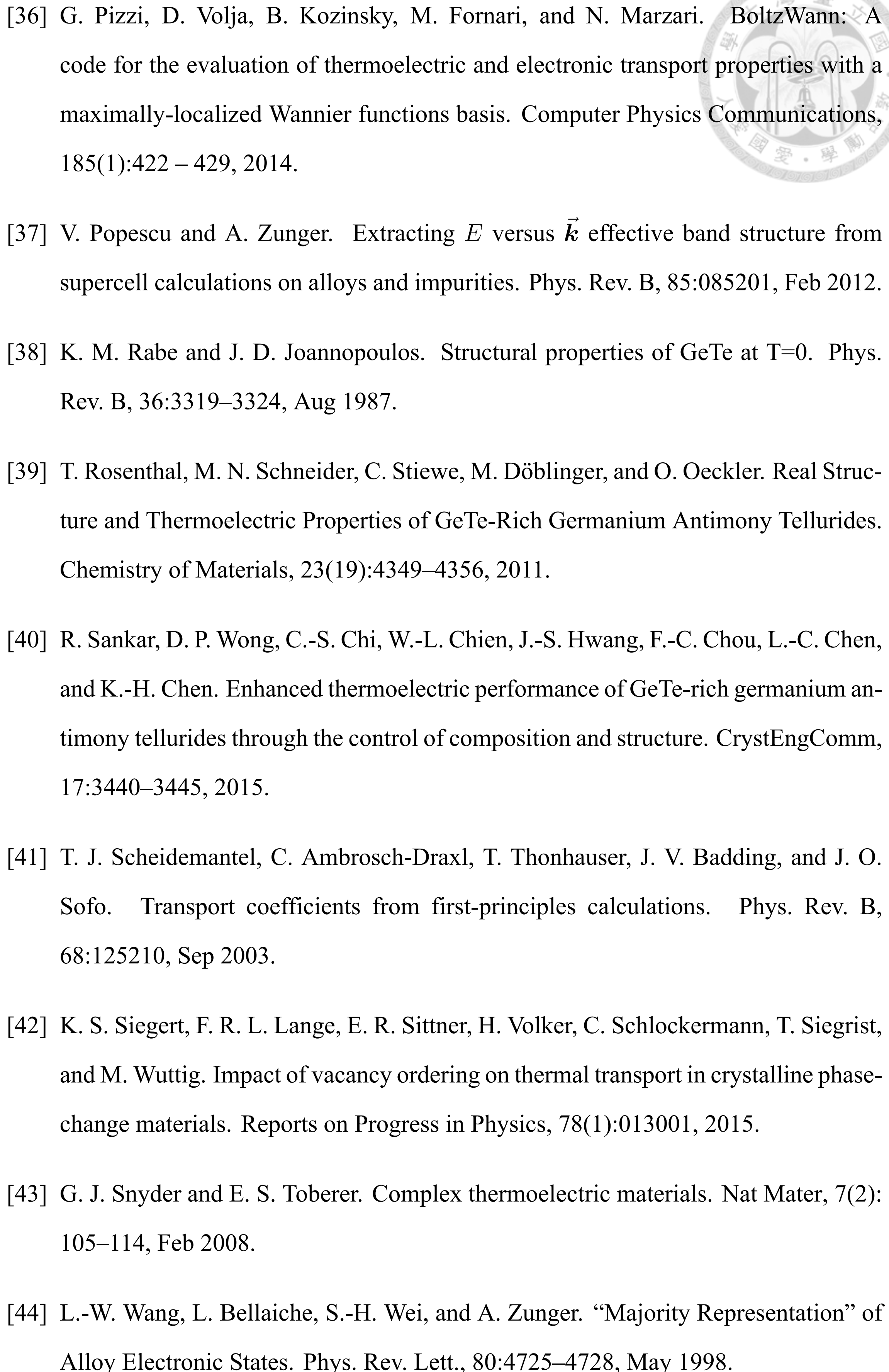

[36] G. Pizzi, D. Volja, B. Kozinsky, M. Fornari, and N. Marzari. BoltzWann: A code for the evaluation of thermoelectric and electronic transport properties with a maximally-localized Wannier functions basis. Computer Physics Communications, 185(1):422 – 429, 2014.

[37] V. Popescu and A. Zunger. Extracting E versus $\vec{k}$ effective band structure from supercell calculations on alloys and impurities. Phys. Rev. B, 85:085201, Feb 2012.

[38] K. M. Rabe and J. D. Joannopoulos. Structural properties of GeTe at T=0. Phys. Rev. B, 36:3319–3324, Aug 1987.

[39] T. Rosenthal, M. N. Schneider, C. Stiewe, M. Döblinger, and O. Oeckler. Real Structure and Thermoelectric Properties of GeTe-Rich Germanium Antimony Tellurides. Chemistry of Materials, 23(19):4349–4356, 2011.

[40] R. Sankar, D. P. Wong, C.-S. Chi, W.-L. Chien, J.-S. Hwang, F.-C. Chou, L.-C. Chen, and K.-H. Chen. Enhanced thermoelectric performance of GeTe-rich germanium antimony tellurides through the control of composition and structure. CrystEngComm, 17:3440–3445, 2015.

[41] T. J. Scheidemantel, C. Ambrosch-Draxl, T. Thonhauser, J. V. Badding, and J. O. Sofo. Transport coefficients from first-principles calculations. Phys. Rev. B, 68:125210, Sep 2003.

[42] K. S. Siegert, F. R. L. Lange, E. R. Sittner, H. Volker, C. Schlockermann, T. Siegrist, and M. Wuttig. Impact of vacancy ordering on thermal transport in crystalline phase-change materials. Reports on Progress in Physics, 78(1):013001, 2015.

[43] G. J. Snyder and E. S. Toberer. Complex thermoelectric materials. Nat Mater, 7(2): 105–114, Feb 2008.

[44] L.-W. Wang, L. Bellaiche, S.-H. Wei, and A. Zunger. “Majority Representation” of Alloy Electronic States. Phys. Rev. Lett., 80:4725–4728, May 1998.

doi:10.6342/NTU201701378

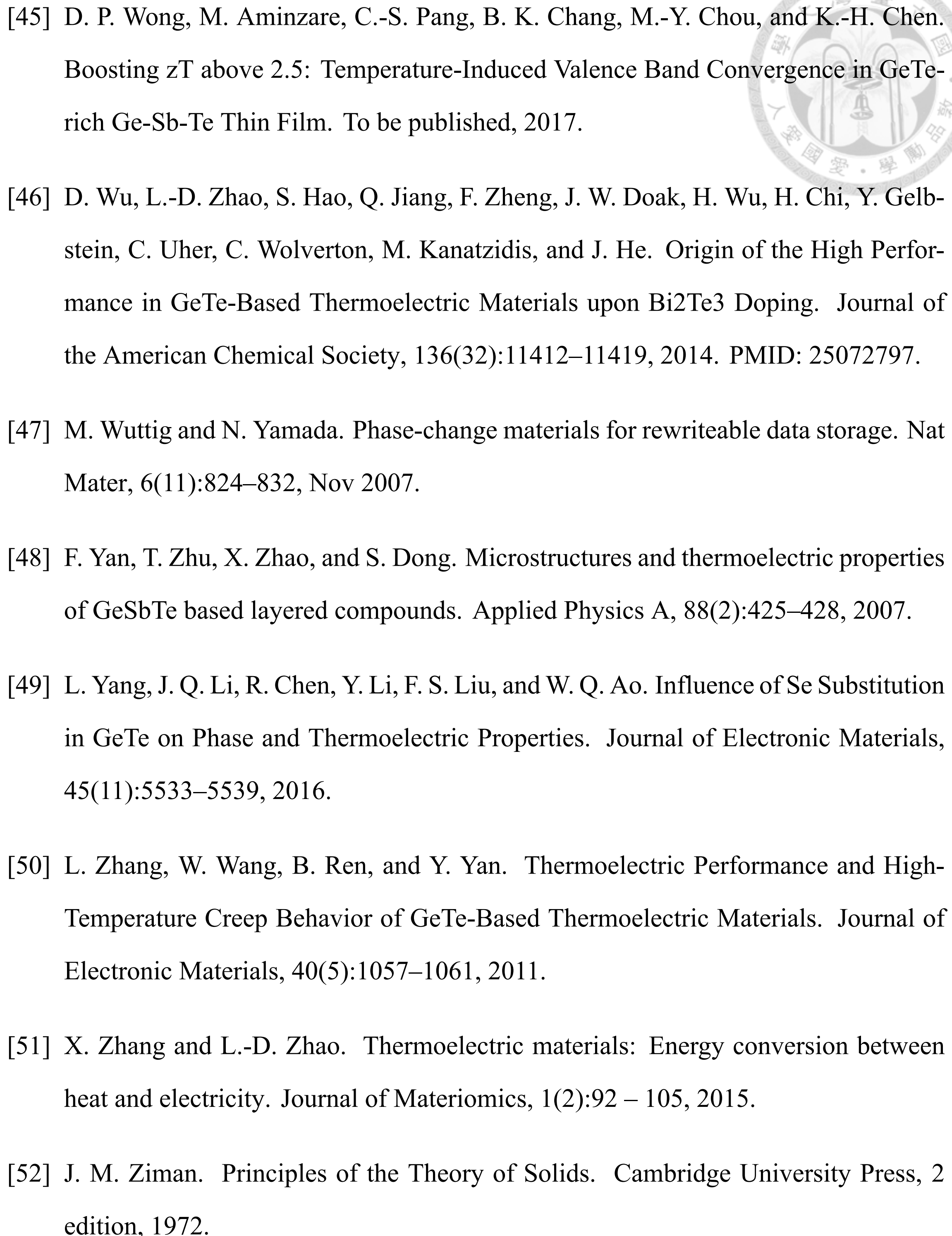

[45] D. P. Wong, M. Aminzare, C.-S. Pang, B. K. Chang, M.-Y. Chou, and K.-H. Chen. Boosting zT above 2.5: Temperature-Induced Valence Band Convergence in GeTe-rich Ge-Sb-Te Thin Film. To be published, 2017.

[46] D. Wu, L.-D. Zhao, S. Hao, Q. Jiang, F. Zheng, J. W. Doak, H. Wu, H. Chi, Y. Gelbstein, C. Uher, C. Wolverton, M. Kanatzidis, and J. He. Origin of the High Performance in GeTe-Based Thermoelectric Materials upon Bi2Te3 Doping. Journal of the American Chemical Society, 136(32):11412–11419, 2014. PMID: 25072797.

[47] M. Wuttig and N. Yamada. Phase-change materials for rewriteable data storage. Nat Mater, 6(11):824–832, Nov 2007.

[48] F. Yan, T. Zhu, X. Zhao, and S. Dong. Microstructures and thermoelectric properties of GeSbTe based layered compounds. Applied Physics A, 88(2):425–428, 2007.

[49] L. Yang, J. Q. Li, R. Chen, Y. Li, F. S. Liu, and W. Q. Ao. Influence of Se Substitution in GeTe on Phase and Thermoelectric Properties. Journal of Electronic Materials, 45(11):5533–5539, 2016.

[50] L. Zhang, W. Wang, B. Ren, and Y. Yan. Thermoelectric Performance and High-Temperature Creep Behavior of GeTe-Based Thermoelectric Materials. Journal of Electronic Materials, 40(5):1057–1061, 2011.

[51] X. Zhang and L.-D. Zhao. Thermoelectric materials: Energy conversion between heat and electricity. Journal of Materiomics, 1(2):92 – 105, 2015.

[52] J. M. Ziman. Principles of the Theory of Solids. Cambridge University Press, 2 edition, 1972.

doi:10.6342/NTU201701378